

## Section 3. Seismic Reflection Amplitude

### Objective:

1. Provide rules-of-thumb for reflection amplitude associated with various shapes of geologic boundaries
2. Present reflection-coefficient equations that separate lithologic from pore-fluid contributions to the AVO response

After loading the seismic data on the workstation, one of the first questions an interpreter asks the data processor is: “What’s the polarity?” The processor assures the interpreter that the final seismic has true-amplitude processing with a zero-phase wavelet, so that a peak represents a reflection from a high-velocity bed. Knowing the complexities that mother earth can introduce, and having a little bit of processing experience, seasoned interpreters are often heard mumbling quotes such as, “It’s your dream, tell it the way you want to.”

But even if the processor has produced his dream section, there are amplitude and phase anomalies that are often not associated with rock type or pore-fluid changes. Once these anomalies are reconciled, reflection amplitudes both on the stack and within CDP gathers can be investigated for rock type and pore-fluid predictions. These predictions from the amplitude interpretation are normally conducted using simplified versions of the reflection-amplitude equation. Which equation is employed depends on what the interpreter is trying to emphasize.

### 3A. Normal-Incident Amplitude

#### *Polarity Issues*

A variety of geophysical receivers are used by the oil industry to measure the particle motion of seismic waves. Likewise, these receivers can be planted on land, towed as streamers, deployed in vertical cables, or planted on the ocean bottom. With respect to polarity, two issues arise: type of receiver, and direction of wavefront.

Particle-velocity geophones and pressure-sensitive hydrophones are the two receivers commonly employed in seismic. Starting with a displacement wavelet, the amplitude relationship between a particle-velocity phone and a hydrophone is shown in Fig. 3.A.1. The theory is based on plane-wave propagation, which is a good approximation for the far-field signature. The strain can be found by taking the partial derivative of the displacement wavelet as a function of the spatial coordinate. Likewise the particle-velocity wavelet is found by taking the partial derivative of the displacement wavelet as a function of time. Note that  $v_x$  is particle-velocity motion while  $V$  refers to propagation velocity; i.e.  $V=5000$  ft/s for water.

Next, Hooke’s Law is called upon to relate stress to strain through an elastic constant  $E$ . The final step in the pressure development requires  $V=(E/\rho)^{1/2}$ . Finally, the theoretical pressure signature is the negative of particle velocity modified by the acoustic impedance.

As mentioned earlier, the direction of the wavefront needs to be considered when analyzing amplitude. As shown in the bottom of Fig. 3.A.2, the signature that a particle-velocity phone records depends on the direction that the wavefront takes. Pressure phones are insensitive to the wavefront direction. Likewise, the placement of the receiver influences the recorded amplitude. If pressure phones were allowed to float on the water surface, they would record amplitudes very near zero. However, particle-velocity phones located on the earth's surface record twice the amplitude of waves approaching the surface vertically. Because pressure phones must be located beneath sea level, they are normally positioned so that the initial upcoming wave is reinforced with the negative reflection from the wave reflected downward from the air-water interface. This pressure-phone phenomenon is called a ghost. A ghost basically introduces a 90°-phase shift with respect to the upcoming wave. The marine source, which is also beneath the surface, can produce another ghost, so that the total effect is a 180°-phase shift.

To add to the confusion of phase determination, there are two polarity standards in common usage (Fig. 3.A.3). Brown (1999) refers to them as the “American” and “European” polarities. Rather than rely on the notation American or European, most interpreters want statements such as “Positive values on the tape are reflections from a hard boundary.” Even with this notation, interpreters still need to confirm the polarity by tying synthetics to the seismic, examining reflections from the ocean bottom, evaluating obvious shallow thin-bed gas zones, etc. More correctly, the statement should be, “Interpreters need to verify the phase of the data.” Marine data, especially older vintage, are notoriously 90° (+ or –) out-of-phase from the desired zero-phase wavelet.

### *Reflection and Transmission Coefficients*

By applying the boundary conditions of continuity of vertical displacement and stress, the equations for normal-incident reflection and transmission coefficients as shown in Fig. 3.A.4 can be derived. The reflection coefficient is the difference of acoustic impedances ( $\rho\alpha$ ) over the sum of the acoustic impedances of the two bounding media. The reflection and transmission coefficients are dimensionless because the respective amplitudes have been normalized to the incident-wave amplitude. The reflection coefficient has values between –1.0 and +1.0, but the seismic range is usually between –0.3 and 0.3.

One aspect of the reflection coefficient that hasn't been mentioned is the reference coordinate system. Is the positive  $z$ -axis pointing upward or downward? If a fixed-coordinate system is selected, then the normal-incident ( $NI$ ) equation will only be true for the particle-velocity or pressure—not for both. Also, it becomes more confusing when amplitude for oblique raypaths are considered in a fixed-coordinate system. To avoid this confusion, the coordinate system is assumed to have the positive  $z$ -axis pointing in the direction of the ray path being considered. Then a positive amplitude particle-velocity wavelet traveling downward will reflect from a hard boundary and travel upward as a positive-amplitude particle-velocity wavelet. The same is true for a pressure wavelet.

The transmission coefficient can also be written as  $(1 - \text{reflection coefficient})$ . However, this is only true for particle-velocity phones if the coordinate system is defined as suggested. For pressure phones, the particle-velocity amplitudes need to be modified by the acoustic impedance of the medium in which the wave is traveling. When this is done, the transmission coefficient for pressure phones is expressed as  $(1 + \text{reflection coefficient})$ .

While the reflection-coefficient expression in Fig. 3.A.4 is the one most often quoted, alternate forms are given in Fig. 3.A.5. The first equation expresses the reflection coefficient as a function of two variables, the velocity and density ratios of the two media. The second equation indicates the amount that the velocity and density contrasts individually contribute to the total reflection. The right side of the second equation indicates that the reflection coefficient can be expressed as a difference ( $\Delta$ ) of the two media properties over the average.

The third expression comes from the approximation,  $\Delta[\ln(\rho\alpha)] \approx [\Delta(\rho\alpha) / \rho\alpha]$ . If the natural log of an acoustic impedance curve is plotted, then the ratio of one reflection amplitude to another can be found by graphically measuring the excursion at each boundary and taking the ratio. This concept is expanded in the fourth equation to graphically illustrate the contributions of velocity and density to the total reflection coefficient. Fig. 3.A.6 contains an example.

The sand formation, which is in the middle of the well-log plot (Fig. 3.A.6), has a higher velocity but a lower density than the encasing shale. However, the scales for the sonic and density curves are deceiving in that it appears that the velocity increase will be cancelled by the density decrease at the upper boundary of the sand formation. A quick visual evaluation is made from the natural logarithm plot on the right. The length of the line  $NI_{vel}$  in the figure is a graphical representation of the velocity contribution to the normal-incident reflection coefficient. The line's origin is at the center of the upper medium's cluster of shale points and vertically goes to the middle of the sand cluster.  $NI_{vel}$  is positive for this reflection, while  $NI_{Den}$  is negative. In this example, the negative contribution of the density,  $NI_{Den}$ , is only one-sixth the magnitude of the positive contribution of the velocity,  $NI_{vel}$ .

### 3B. Geometric Considerations of Amplitude

#### *Wavelets Reflected from Geologic Boundaries*

While the processor promised zero-phase seismic data, trying to find this wavelet shape in the seismic data is similar to finding a needle in a haystack. On most seismic sections, flat-lying, thick constant-velocity beds that produce zero-phase reflections are seldom observed. Seismic data consist of a “convoluted” form of various wavelet shapes; some are easy to predict—others not so easy. A few of the predictable wavelet shapes are shown in Fig. 3.B.1. Starting with the basic zero-phase wavelet, the integral, 1<sup>st</sup> derivative and 2<sup>nd</sup> derivative, wavelet shapes are cartooned.

The time on the wavelet that is associated with the reflection is indicated by the reference 0 at the bottom of the figure. The integral and 1<sup>st</sup> derivative shapes have the

reflection time at a zero-crossing point. The integral has the lowest apparent frequency content and the frequency content increases steadily from the integral to the 2<sup>nd</sup> derivative.

If the thick-bed response is the shape of the basic wavelet, then other wavelet shapes will exist for reflections from:

thin bed	1 <sup>st</sup> derivative
refraction	integral
velocity gradient	integral
small area	1 <sup>st</sup> derivative
small volume	2 <sup>nd</sup> derivative
buried-focus syncline	90°-phase change
buried-foci basin	180°-phase change

Of course, each of the above is also associated with an amplitude change.

The variation from the basic wavelet shape results from either a vertical change in the acoustic impedance or a lateral change from a flat boundary. If 3-D seismic is employed, then the phase variation associated with nonflat boundaries will revert to zero-phase after 3-D migration. However, a 2-D line across any of the last four geometric shapes listed can lead to some perplexing wavelet shapes and reflection patterns after migration. This is introduced as a warning when amplitude interpretation is based on an extracted 3-D line that is 2-D processed.

### *Thin-Bed and Transitional Velocity Responses*

Wavelet changes associated with vertical variations in acoustic impedance are illustrated in Fig. 3.B.2. For simplicity, the density curve was held constant in this model. There are three factors to consider for each reflection sequence. They are the reflection event timing, the additional amplitude scalar over the reflection coefficient, and the shape of the wavelet. In the 1-D synthetic, the velocity curve was selected so that the velocity ratio and thus the reflection coefficients are the same for each bed response. The principle being illustrated is, "If a thick bed has a reflection amplitude of one (1), what additional scalar is needed for a thin-bed or transitional velocity change?"

In a classic paper by Widess (1973), the thin-bed response shown in Fig. 3.B.2 was given. Widess was awarded the Virgil Kauffman Gold Medal for the significance that this paper had on stratigraphic interpretation using amplitude. When the thickness of a bed is less than one-eighth of the seismic wavelength (computed with the interval velocity of the thin bed), the composite reflection amplitude is directly proportional to the thickness of the bed. The composite reflection takes the shape of the derivative of the zero-phase wavelet. That assumes zero-phase processing.

When the bed thickness is greater than one-fourth the wavelength, thickness estimates are determined from the time interval measured between the reflections from the top and bottom. Essentially, the reflections are resolvable in time. Time and amplitude analyses of thin beds are often referred to as TAMP. Two TAMP examples are given in Fig. 3.B.3. The wedge model on the left was generated with a zero-phase Ricker

wavelet, and the one on the right with a minimum-phase wavelet. The time separation between the upper and lower reflections varies continuously from 45 ms to 1 ms. In both models, the maximum peak-to-trough amplitude occurs at the tuning thickness of  $\lambda/4$ . For the Ricker model, the time separation between the peak and trough decreases linearly until the tuning thickness is reached, and then the peak-trough time separation remains essentially constant. The time-interval and amplitude plots for the minimum-phase wavelet are not as smooth as the Ricker-wavelet example because of the *ringing* nature of the specified minimum-phase wavelet.

In TAMP analyses, one uses time separation to estimate thick beds and amplitude to estimate thin beds. However, additional information or assumptions are necessary in order to relate amplitude to thickness. For instance, the interval velocity of the thin bed and the reflection coefficients at the top and base of the thin bed are needed for comparison to background reflections. Neidell and Poggiagliolmi (1977) detailed the principles and assumptions of thin-bed analyses with practical examples. Neff's (1992) incremental pay thickness modeling was an extension of thin-bed analysis for 3-D data that led to reservoir pay volume and pay distribution estimates.

Besides TAMP, several authors proposed techniques for estimating thickness in the frequency domain. Fig. 3.B.4 contains amplitude spectra for each trace of the wedge models in Fig. 3.B.3. The thickness of the bed (in two-way traveltime) can be estimated in the frequency domain by noting the periodicity of the notches in the amplitude spectra. In the figure, the spectra associated with 45-ms thickness have notches at approximately 22, 44, and 66 Hz. This corresponds to the time-frequency relationship of  $1/45 \text{ ms} = 22.22 \text{ Hz}$ . As the bed thickness decreases, the spectral notches move to higher frequencies. With this notch movement, the amplitude-spectra contour plots in the bottom of the figure illustrate the difficulty of estimating thickness with frequency analyses. The contours are essentially the same for the thickness interval from 0 to  $\lambda/4$ . Thus differentiating 20-ft (6-m) thick beds from 40-ft (12-m) ones would be questionable using the shape of amplitude spectra.

Because the minimum-phase wavelet was designed with a flat band-pass spectrum, the derivative effect of the thin bed can be observed. In the right plot, the high-frequency content increases as the bed separation approaches zero thickness. The amplitude spectra in Fig. 3.B.4 were normalized to the same maximum value.

The counterpart to a thin bed is a transitional- or ramp-velocity layer. This is shown in the bottom portion of Fig. 3.B.2. Its theoretical response can be derived in a fashion similar to Widess's (1973) development, or a heuristic approach can be used. When the reflectivity series for a thin bed  $[\delta(t) - \delta(t-\Delta t)]$  is convolved with the reflectivity series of a ramp [unit-step function], a spike results at the top and base of the ramp. In order to achieve this, the ramp must compensate for the thin-bed effect. To do this, the ramp has an integral wavelet shape and a scalar that is inverse to the thin-bed scalar.

While the concept of amplitude associated with thin-bed effects received new attention in the mid-1970s, previous work had been published. Basically, the principles presented in Figs. 3.B.1 through 3.B.3 were elegantly developed by Sengbush et al. in 1961. However, it took the digital-recording revolution and the concepts of "true" amplitude processing to awaken our industry to these benefits.



### *Small-Area and Small-Volume Responses*

An amplitude-interpretation falsehood of the early 1970s was put to rest by Widess's (1973) paper. No longer was it thought that thin beds were invisible to the seismic method. In a similar fashion, the argument that a geologic structure must have an areal extent of one Fresnel zone or it will be seismically invisible, still exists to some extent. In Fig. 3.B.5, the unmigrated seismic response of a small area is seen to take the same wavelet shape and scalar form as a thin bed. An example of a small-area response is a reflection from the top of a volcanic dike.

Hilterman (1982) showed that the small-area response was approximately  $[\delta(t) - \delta(t - \Delta t)]$ , where  $\Delta t$  was the two-way traveltime difference between a reflection to the center of the small area and a diffraction from the average edge. This combination of a specular reflection and diffraction from a small area has the same impulse response as a thin-bed. In short, a Fresnel zone is not necessary to support a reflection. A small area will have a seismic response that linearly decreases in amplitude as the area size decreases. The small-area response has a tuning area similar to the tuning thickness for a thin bed.

The extension to a small volume is obtained by applying a thin-bed response to a small-area response. The scalar for the small volume is the product of the small-area scalar and the thin-bed scalar. The small-volume composite shape is the derivative (thin bed) of a derivative (small area) to yield the second-derivative effect.

### *Amplitude, Phase, and Timing Distortions*

If a geologic structure is not flat, the amplitude on unmigrated seismic data will be affected by the structure's shape. The scalar and phase introduced by geometric shapes was summarized by Hilterman (1975) and is shown in Fig. 3.B.6. The shape of a geologic surface can be approximated with two principal radii of curvature. The equations in the figure apply to one principal plane. As an example, let the structure be a 2-D anticline with a seismic line traversing the dip direction. If the top of the anticline is buried at 5000 ft (1500 m) and the anticline's radius of curvature is 3000 ft (900 m), the reflection off the top of the anticline will have an amplitude that is reduced from a flat reflection at the same depth by the factor  $[1/1+5000/3000]^{1/2}$ . The anticline's amplitude will be 0.6 that of an equivalent flat bed. Of course, migration will restore the anticline's reflection amplitude to 1.

However, if the geologic structure is not 2-D in shape, then the out-of-plane response is applied as indicated in the bottom of the figure. Thus, for our example, if the geologic structure is a dome with a radius of curvature of 3000 ft, the resulting amplitude off the top of the structure will be 0.36. 2-D migration will restore the amplitude to 0.60. Thus, amplitude ratios for predicting pore-fluid content that compare top of the structure reflections to downdip reflections will be biased by 3-D geometry. The problem becomes more complicated for negative structures as phase distortions and extra events (sideswipe) become involved. A couple of examples will illustrate these unwanted effects.

Seismic lines were generated across a syncline and a basin (Fig. 3.B.7). The syncline

and basin have the same cross-sectional shape in the plane of the seismic lines. The syncline has 2-D curvature while the basin has 3-D. The same syncline and basin were modeled at two different depths, 1500 ft (450 m) and 7500 ft (2300 m). The seismic lines were 2-D migrated and are shown in the lower portion of the figure. For the 1500-ft depth, the migrated sections for the basin and syncline are nearly the same. However for the 7500-ft depth, the basin displays an additional reflection that is associated with the out-of-plane lip of the basin. Though it is difficult to see on these figures, the amplitude in the basin is significantly higher than it should be, due to focusing.

The next examples in Fig. 3.B.8 are even more discouraging. The previous example was modeled with a seismic line through a principal plane. A principal-plane seismic line exists if a mirror is placed vertically through the seismic line, and the mirror image is exactly what exists if the mirror is removed. Lines B and C do not go through a principal plane. The false interpretations shown on the 2-D migrated sections include extra faults, extra events, and amplitude and phase distortions.

Though basins are not favorite structures to drill, deposits on the sides of shale diapers and salt domes have “basin-type” shapes that are tilted and enjoy all the unpleasant seismic effects if 2-D seismic is used for amplitude interpretation. The warning is repeated: if 2-D processing is applied, then potential amplitude and phase distortions, extra events, and erroneous faults caused by 3-D geometry must be reconciled. That’s a tough assignment.

### *Multi-Boundary Relationships*

Often, a clue to the magnitude and polarity of a reflection event can be obtained near a geologic pinchout. As shown in Fig. 3.B.9, the reflection coefficients associated with the boundaries that meet at the truncation point are not independent. Reflection coefficient  $R_3$  is approximately equal to the algebraic sum of  $R_1$  and  $R_2$ . If all the reflection coefficients are the same polarity, then  $R_3$  will be “brighter” than  $R_1$  and  $R_2$ . In short, an increase in amplitude is not necessarily an indication of hydrocarbons, even though it may be appropriately situated geologically.

On the right of the figure, formations are shown encased between two beds that have the same acoustic impedance. For this situation, the reflection coefficients ( $R_1$  to  $R_4$ ) algebraically sum to zero (approximately). When analyzing a bright spot that is thought to be encased in shale, top and bottom reflections of equal magnitude should be observed, otherwise a derivative of the basic wavelet is expected. If this is not the case, then vertical variations in the acoustic properties of the reservoir should be suspected.

### **3C. Amplitude Versus Incident Angle**

The normal-incident reflection coefficient equation was the mainstay for amplitude interpretation for numerous years. Now, amplitude interpretation includes AVO. In 1955, Koefoed presented five observations relating the shape of the AVO curve to changes in Poisson’s ratio. These observations led Koefoed to advocate that lithology could be extracted from seismic data. His observations will be discussed later.

However, it was Ostrander's (1982) AVO verification with field data and successful exploration wells that spurred geophysicists to examine AVO. These AVO origins are captured in Fig. 3.C.1 by statements from the two pioneers.

Not listed in Fig. 3.C.1 was Koefoed's first suggestion for the practical application of AVO—that is, use AVO to improve the quality of reflections on a seismogram by a judicious choice of the distance from the shotpoint to the seismometers. With the expansion of the number of recording channels, this suggestion has had limited application. Likewise, his second comment about using AVO as a correlation tool is often underutilized by interpreters. If synthetic seismograms had been invented at the time of Koefoed's article, his statement might have read, "Whenever a 1-D synthetic doesn't correlate with the field seismic, correlate the synthetic AVO response to the migrated CDP gathers at the well location." This is especially helpful for areas with young clastic sediments at shallow depths. In these areas, the difference in Poisson's ratio between the lithologies is a more robust expression of the AVO character than the small changes in the acoustic impedances that drive the normal-incident response. An interesting note about his third statement, which relates lithology to AVO, is that Koefoed predicted this application to occur in the more "remote future." He was right ... 27 years' remote, until Ostrander's presentation.

Ostrander's statement in Fig. 3.C.1 was excellently supported in his 1984 article. The CDP gather in the figure, which shows an increase of amplitude with offset, is from the article and represents the classic signature that all interpreters hope to find over their prospects. In his paper, Ostrander presented the theoretical models, petrophysics, and the required data processing before he discussed three case histories. Likewise, he highlighted the anomalous factors that affect AVO, as warnings to the interpreter. His paper is a mini-course in AVO interpretation.

Immediately after Bill Ostrander made his presentation at the 1982 SEG Annual Convention, plans were formulated to develop his concepts into an SEG Continuing Education Short Course. These notes have their origin in this short course.

### *Fluid-Fluid Interfaces*

It might seem a bit inappropriate to cover reflections from fluid-fluid boundaries, because our objectives of determining pore-fluid content and rock type are associated with solid-solid interfaces. However, the fluid-fluid reflection coefficient equation is an integral part in deciphering pore-fluid effects with AVO.

The fluid-fluid equation given in Fig. 3.C.2, at first glance, appears to be almost a duplicate of the normal-incident reflection coefficient equation except for the cosine terms. However, the equation, though appearing simple, covers post-critical angle reflections. The reflection amplitude for incident angle  $\theta_1$ ,  $RC(\theta_1)$ , is dependent on the transmission (refracted) angle  $\theta_2$ . If the incident angle exceeds  $\sin^{-1}(\alpha_1/\alpha_2)$ , the reflection becomes critical. No transmitted  $P$ -waves exist for incident angles beyond the critical angle. The reflection coefficient past the critical angle has an imaginary part that means the waveform exhibits a phase change. Surprisingly, all this information is contained in the simple fluid-fluid equation.

The amplitude and phase spectra for a fluid-fluid interface are plotted in Fig. 3.C.3. The density contrast is zero between the two media. Past the critical angle of  $33.7^\circ$ , the



amplitude spectrum has a value of 1 and the phase spectrum slowly changes from zero-phase at the critical angle to  $\pi$  ( $180^\circ$ , a phase reversal) at the grazing incident angle of  $90^\circ$ .

What is not indicated on these spectral plots is the head wave (often called the refraction arrival). To observe this, a total elastic synthetic (SOLID, Sherwood et al., 1983) was generated for the same model in Fig. 3.C.3 and this is plotted in Fig. 3.C.4. The model was generated with an upper half-space medium having the same properties as the first layer. This is equivalent to having no air-water interface, or having water up to the moon and towing the source and streamer with a submarine.

The amplitude of the direct arrival in the figure is constant because a constant-velocity spherical-divergence correction was applied to the synthetic. By applying the spherical divergence correction, the amplitudes on the NMO-corrected *PP*-arrival should somewhat correspond to the amplitude spectrum in the previous plot. The NMO (normal moveout) correction is not the conventional NMO, but rather is a static correction that lines up the *PP*-reflection. Correcting the extra moveout time in this fashion does not stretch the waveform, and thus amplitude and phase relationships at various angles can easily be evaluated with respect to the zero-offset reflection. For instance, the last trace on the static shifted event has an incident angle of  $63^\circ$  and the phase spectrum from the previous figure indicates a phase change of approximately  $\pi/2$  ( $90^\circ$ ). The waveform on the last trace has an approximately  $90^\circ$ -phase shift with respect to the basic wavelet at normal incidence. The wavelet on the last trace has a lower frequency content than the wavelet on the first trace, as a result of the array response used in the model. The fluid-fluid synthetic has only three events: direct arrival, *PP*-reflection, and a head wave. The amplitude associated with the head wave for this model is very small.

The shape of the AVO curve for a fluid-fluid interface is not complicated. This is illustrated by the amplitude spectra from four models in Fig. 3.C.5. The four models represent all possible shapes for fluid-fluid reflection spectra. The models were based on permutations of the velocities 5000 and 7000 ft/s (1500 and 2100 m/s) and the densities of 1.0 and 2.0 gm/cm<sup>3</sup>. There are two possible velocity ratios, 0.71 and 1.40, and two density ratios, 0.5 and 2.0. All model permutations are shown. The amplitude responses can be summarized as:

- If the lower-medium acoustic impedance is greater than the upper, the normal-incident reflection is positive, and vice versa.
- If the lower-medium velocity is greater than the upper, the reflection magnitude is one (1) for angles between the critical and grazing incidence ( $90^\circ$ ).
- If the lower-medium velocity is less than the upper, the reflection amplitude monotonically approaches  $-1.0$  at grazing incidence.
- The amplitude spectra increase or decrease monotonically, depending on the velocity ratio.

The fluid-fluid spectra are simple to analyze. Are the solid-solid AVO curves as easy to interpret?

### Solid-Solid Interfaces

With the addition of shear waves, the evaluation of all possible events generated from an incident *P*-wave source onto a single interface quickly becomes complicated. Fig. 3.C.6 illustrates all wavefronts that are generated if the source medium has a *P*-wave velocity that is less than the *S*-wave velocity of the second medium. This is equivalent to having the source in the weathered layer. There are 10 different wavefronts generated. And this is for an isotropic, elastic medium without an air interface to reflect energy downward! If anisotropy is introduced and *S*-wave splitting is allowed, there would not be enough room on the page to label all the possible wavefronts.

Concentrating on the reflected and refracted (transmitted) waves only, Fig. 3.C.7 shows the notation for the principal raypaths for the *P*- and *S*-waves. With the help of Snell's Law, the direction of all raypaths are defined. All that is needed now is to associate amplitudes with each of the four waves generated by the incident *PP* wave.

There are several textbooks that derive these amplitudes and all are prone to some printing error, including authors who note that others have published the incorrect equations. Therefore, following the precedent of assurance of accuracy by others, the equations published by Jakosky (1960) and reproduced in Fig. 3.C.8 are "correct." Once again, the amplitudes for the reflected *P*-wave, *RP*, and *S*-wave, *RS*, can be complex numbers. Computer programs to invert this matrix to yield a complex-number column solution are readily available such as the one provided by Press et al. (1996).

An excellent bible on ray-trace procedures and algorithms is the book by Cerveny and Ravindra (1971). Among other things, they provide explicit expressions for all 16 different reflection coefficients (incident direction downward and upward for *P*-wave and *S*-wave sources). No attempt has been made here to reproduce the explicit *PP* reflection-coefficient expression—it requires more than 80 multiplications and additions. However, the author has compared the matrix-inversion solution against Cerveny's explicit expression for the reflected *PP* amplitude and phase spectra. They yield identical results.

### Solid-Solid Interfaces—Large Velocity Contrasts

For a *P*-wave source, there are eight possible reflected or transmitted waves that can be generated from a solid-solid interface if both the upward and downward incident waves are considered. Fig. 3.C.9 contains the eight magnitude spectra for a geologic model that is an exception for exploration seismic. The *P*-wave velocity of the lower medium is 2.5 times that of the upper *P*-wave velocity. This large *P*-wave velocity contrast creates "interesting" shapes for the reflection-coefficient curves with respect to incident angle. In fact, one of these plots could supply enough information for a PhD dissertation. The following points relate to the coefficient curves in the figure:

- At normal incidence, no shear waves are generated (panels b, d, f, and h).
- No compressional energy enters the lower medium beyond the first critical angle,  $\alpha_c$  (panel c). No shear energy enters the lower medium beyond the second critical angle,  $\alpha_s$  (panel d).

- When the incident direction is reversed (panels e – h), there are no critical angles and the coefficient curves are much smoother.

While there are incident angles that have near total reflection in panel (a), the associated amplitudes do not necessarily appear on the synthetic because of the contribution from head waves that are not taken into consideration on these plots. This can be observed on the total elastic synthetic plotted in Fig. 3.C.10. The same input parameters were used as in Fig. 3.C.9.

The *PP* reflection has once again been aligned using a static shift in order to observe the amplitude and phase relationships along the reflection event. A spherical divergence correction has been applied. At the critical angle of  $23^\circ$ , a large reflection amplitude is predicted from the amplitude spectrum. However, on the synthetic, the head wave interferes destructively with the *PP* reflection so that the high amplitude does not exist. Because  $\beta_2 > \alpha_1$ , a second head wave is also generated. At the very-far offsets, the *PP* reflection changes phase with respect to the normal-incident reflection. As mentioned, this large velocity contrast is an exception rather than the rule for exploration seismic. So let's examine a more realistic geologic model in Fig. 3.C.11.

#### *Solid-Solid Interfaces—Small Velocity Contrasts*

The model in this figure, with a 30% increase in velocity, has coefficient curves that are much smoother than the previous large velocity contrast model. The S-wave velocity of the lower medium is less than the P-wave velocity of the upper, so the second critical angle does not exist. The following are a few generalized points about the coefficient curves:

- Even though the *PP* reflection curve is smooth for small angles, the zero-offset amplitude is almost twice as strong as the  $30^\circ$  amplitude. Large velocity contrasts are not necessary to have significant amplitude variations at the small incident angles.
- The amplitude of the transmitted wave is approximately constant up to the critical angle.
- For small incident angles, the *PP* reflection from beneath the boundary has a shape similar to that of the *PP* reflection from above the boundary. However, they are opposite in polarity.

The total elastic synthetic for this model is shown in Fig. 3.C.12. Statics and a divergence correction have been applied. According to the amplitude spectrum, the reflection should exhibit large amplitude at the critical angle when compared with the normal-incident amplitude. As noted before, this large amplitude does not exist because of the head-wave interference. For postcritical analysis, there are differences between the amplitude spectrum from plane-wave theory and the amplitude response generated from the total elastic solution. For a one-on-one comparison, the amplitudes in the total elastic solution were corrected for spreading loss and direction of emergence ray to a vertical-response phone and the array effect imposed by the modeling program. The

amplitude comparison is presented in Fig. 3.C.13. Well before the critical angle is reached, the ray theory and total elastic amplitudes begin to diverge. With the advent of routine nonhyperbolic NMO corrections, one has to wonder how the amplitudes associated with the very-large offsets will be interpreted. Do we have an amplitude interpretation theory that will handle the nonpredictable zone? The author doesn't have concise equations to deal with these far offsets; however, a case history will be presented later regarding how to deal with these problems using today's interpretation and modeling software.

While there are large variations in the amplitude spectrum associated with critical and postcritical reflections, most amplitude interpretations are conducted well beneath the critical angle. There were several generalized statements made concerning reflection amplitudes for small velocity contrasts, but there are still basic questions unanswered such as the one presented in Fig. 3.C.14. Seismic interpretation is interested in the change in AVO shape as a function of property changes. The property changes in Fig. 3.C.14 represent the lower medium going from a water-saturated state to a gas-saturated state. Is there any advantage in going back to the Zoeppritz matrix in Fig. 3.C.8 and asking what would happen to the *PP* reflection if the lower *P*-wave velocity and density were reduced by 10%? No interpretive insight is gained from this equation. This is why linear approximations to the Zoeppritz equation were developed.

### 3D. Linear Approximation of Zoeppritz's Equation

In 1961, Bortfeld derived several formulae for calculating reflection and transmission coefficients as a function of incident angle. He claimed that his approximations of Zoeppritz's equations were accurate to within a few degrees of the critical angle. His formulae for the reflected *PP* and *PS* coefficients are shown in Fig. 3.D.1. The *PP* equation has been modified to remove the natural logarithms from his original equation, but the modified equation yields essentially the same result as the original formula.

An important aspect of Bortfeld's equations is the insight that they provide the interpreter in predicting how amplitude varies with offset as a function of rock properties. The first term in Bortfeld's *PP* equation is the fluid-fluid reflection coefficient equation that was discussed earlier. The second term has been called the rigidity term because of its dependence on the *S*-wave velocity, and thus on the shear-rigidity modulus. There are three special cases to examine in the Bortfeld approximation. They are:

- If  $\beta_1 = \beta_2 = 0$ , the fluid-fluid case, the rigidity term goes to zero;
- If  $\beta_1 = \beta_2$  and  $\rho_1 = \rho_2$ , then once again the rigidity term goes to zero; and
- If  $\rho_1 = \rho_2$ , the rigidity term factors to  $2[\sin(\theta_1)/\alpha_1]^2 [\beta_1^2 - \beta_2^2]$ .

In order to illustrate the interpretive benefits of Bortfeld's work and to correlate his work to petrophysics, a model based on rock properties from the Gulf of Mexico (GOM) was developed, rather than selecting arbitrary velocities and densities.

### Rock-Property Model

Shale velocity and density trend curves were generated from well-log curves in the GOM. At 4000-, 9000-, and 14,000-ft depths (1200-, 3000-, and 4000-m depths), sand velocities were selected to yield shale-over-sand reflection amplitudes that are negative, near zero, and positive. As will be discussed in more detail later, these reflection amplitudes correspond to Class 3 (bright spot), 2 (phase reversal), and 1 (dim out) AVO anomalies, respectively. The density values of the sands were selected from GOM velocity-density crossplots. Gas was fluid substituted into these sands using the Greenberg-Castagna method, with fluid properties from Batzle and Wang. The water-saturated and gas-saturated rock properties for the three depth intervals are given in Fig. 3.D.2. The three models will be used throughout this book to illustrate amplitude-interpretation principles.

### Analysis of Bortfeld's Equations

Bortfeld AVO responses were generated for the water-saturated and gas-saturated models at 9000 ft (3000 m). The results are plotted in Fig. 3.D.3. Each plot contains four curves. The green-triangle curve represents the rigidity term; blue plus signs, the fluid term; brown squares, the total Bortfeld response; and black line, the exact Zoeppritz solution.

For the water-saturated and gas-saturated scenarios shown in Fig. 3.D.3, the Bortfeld approximation is quite close to the exact Zoeppritz solution, which is plotted as the black curve. What is interesting is the similarity of the rigidity term for the wet and gas cases. They are almost identical. This implies that the difference between a water-saturated AVO response and the respective gas-saturated AVO response lies solely with the fluid term. Stated another way, *Only the acoustic impedance is necessary to differentiate pore-fluid content.* This is not surprising, though. The rigidity term depends mainly on the S-wave velocities, and these aren't appreciably influenced by the pore-fluid content. This emphasizes why an understanding of the shape of the reflection coefficient curve for the fluid-fluid AVO response is essential. If the pore-fluid content is determined from the fluid-fluid term in Bortfeld's equation, what is the significance of the rigidity term?

In order to gain some insight to this last question, AVO responses from the Bortfeld approximation are shown in Fig. 3.D.4 for the shallow and deep models. Once again, the rigidity curves are approximately the same for the water-saturated state and the gas-saturated state.

One conclusion can be reached when the AVO responses from the three depth models are compared: the normal-incident amplitude difference between the water-saturated state and the gas-saturated state commonly decreases with depth.

If the rigidity curves for the three depth models are compared, it is noted that the slope of the rigidity curve increases with depth. This occurs because the rock-property model was developed for a basin in which the P-wave velocity of sand becomes faster than shale as a function of depth. With sand normally having a smaller  $V_P/V_S$  ratio than shale, the difference in S-wave velocities between shale and sand increases with depth.



This also represents going from unconsolidated sands at shallow depths to more consolidated sands at deeper depths.

What is disappointing about the Bortfeld approximation is its inaccuracy for incident angles approaching  $30^\circ$  for the 14,000-ft depth model. The exact Zoeppritz solution (black curve) for the water-saturated model at 14,000-ft depth indicates that the amplitude at  $30^\circ$  would be approximately 33% of the normal-incident amplitude, while the Bortfeld approximation predicts zero amplitude at  $30^\circ$ . This magnitude of error is definitely within the resolution of seismic data. This suggests that the exact Zoeppritz equation should be used for ray-trace modeling—a suggestion that will be refuted later.

### *AVO Relationship to Rock Moduli*

The significance of the fluid term in Bortfeld's equation can be related to Gassmann's equation, as depicted in Fig. 3.D.5. Gassmann's equation was previously expressed in terms of the moduli for the dry-rock components and for the pore-fluid component. Values for these moduli for the 4000-ft depth and 14,000-ft depth models are given in the figure.

For the 4000-ft model, the water-saturated pore-fluid contribution (5.4 GPa) is of the same order of magnitude as the total dry-rock modulus (4.22 GPa). When the rock is gas saturated, the pore contribution reduces to approximately 0.3 GPa. Thus, changes in the pore-fluid moduli change the total moduli by almost 100%. The rock begins to act as a suspended load (unconsolidated) and Wood's fluid equation holds. Thus, changes in the fluid factor dominate the AVO response.

At the 14,000-ft depth, the pore-fluid contribution (2.4 GPa) is insignificant when compared with the dry-rock moduli (36.85 GPa). Now, the pore fluid contributes little to the total rock moduli for either the gas- or water-saturated model; the dry-rock moduli are the dominant components.

Bortfeld's introduction of the fluid-fluid and rigidity terms provided rock-property insight on how the AVO curves change during pore-fluid substitution. However, this occurred only after the AVO curves were computer generated. The fluid-fluid and rigidity terms themselves are still a bit difficult to evaluate mentally. Yanghua Wang (1999) expressed Bortfeld's equation in a form that is quite instructive (Fig. 3.D.6). His notation, along with other authors' notations for the linear-approximation equation, is included in Table 1. Wang's expression for the fluid-fluid term indicates that only the  $P$ -wave velocity can change the way the amplitude increases or decreases with offset in fluid-substitution models. The density contribution is flat. In the rigidity term,  $\Delta\mu$  is the same for the hydrocarbon- and water-saturated states. The term  $\sin^2(\theta)/\alpha^2$  is the square of the ray parameter,  $p$ , and this basically remains the same for hydrocarbon- or water-saturated states. The only change that the rigidity term offers during fluid substitution is through the change of the average density,  $\rho$ , which is a small change.

In order to simplify Bortfeld's equation, Wang introduced the elastic constant,  $\mu$ , rather than using exclusively velocity and density variables. Other authors have suggested this change in variables also. With Gardner's strong petrophysical contributions to literature, it was a natural that Gardner and Forel (1987) advocated expressing the AVO response in terms of rock moduli rather than  $P$ -wave and  $S$ -wave velocities.

Gardner and Forel's linear approximation to Zoeppritz's equation is expressed as:

$$\cos^2(\phi) RC(\theta) \approx \frac{1}{4}[\Delta\rho/\rho + \frac{1}{4} \Delta M/M] - [\frac{1}{2} \Delta\rho/\rho + 2\Delta\mu/M] \sin^2(\theta) + [2\Delta\mu/M] \sin^4(\theta) \quad [21]$$

This emphasis of expressing the reflection-coefficient equation in terms of the elastic constants has started to gain additional support with the introduction of  $\lambda\rho$  and  $\mu\rho$  AVO attributes by Goodway et al. (1997).

**Table 1. Rock-Property Notation**

$RC(\theta)$  = reflection amplitude for incident angle  $\theta$

Subscript 1 refers to upper medium, 2 to lower medium

$\Delta\alpha$  = difference in *P*-wave velocity =  $\alpha_2 - \alpha_1$

$\Delta\beta$  = difference in *S*-wave velocity =  $\beta_2 - \beta_1$

$\Delta\rho$  = difference in density =  $\rho_2 - \rho_1$

$\Delta\sigma$  = difference in Poisson's ratio =  $\sigma_2 - \sigma_1$

$\Delta M$  = difference *P*-wave modulus =  $M_2 - M_1$

$\Delta\mu$  = difference *S*-wave modulus =  $\mu_2 - \mu_1$

$\alpha$  = average *P*-wave velocity =  $(\alpha_2 + \alpha_1)/2$

$\beta$  = average *S*-wave velocity =  $(\beta_2 + \beta_1)/2$

$\rho$  = average density =  $(\rho_2 + \rho_1)/2$

$\sigma$  = average Poisson's ratio =  $(\sigma_2 + \sigma_1)/2$

$M$  = average *P*-wave modulus =  $(M_1 + M_2)/2$

$\mu$  = average *S*-wave modulus =  $(\mu_1 + \mu_2)/2$

$\theta = \theta_1$  = incident angle

$\theta_2$  = refracted or transmitted angle

$\phi$  = average of incident and transmitted angles

In Shuey's equation:

$NI_P = \frac{1}{2}[\Delta\alpha/\alpha + \Delta\rho/\rho]$

$A_0 = B - 2(1+B) [(1-2\sigma)/(1-\sigma)]$

$B = [(\Delta\alpha/\alpha) / (\Delta\alpha/\alpha + \Delta\rho/\rho)]$

### *Linear Approximations of Zoeppritz's Equation*

There are numerous expressions for the linear approximation of Zoeppritz's equation, each with a different emphasis. Gardner's was on rock moduli. Three others are shown in Fig. 3.D.7. Bortfeld's equation is shown in its original form with the natural logarithms along with Aki and Richards's (1980) and Shuey's (1985) equations. Although not referenced as often, Richards and Frasier in 1976 published the linear-approximation equations that appear in Aki and Richards's book.

While Bortfeld's emphasis on the fluid and rigidity terms provided insight when interpreting fluid-substitution problems, Aki and Richards's equation emphasizes the contribution of variations in the  $P$ - and  $S$ -wave velocities and density. Shuey, after learning about the contributions of Koefoed and the amplitude dependence on Poisson's ratio, decided to cast Aki and Richards's equation in terms of Poisson's ratio. In addition, he showed which combinations of rock properties were effective at successive ranges of incident angles. The Poisson's ratio dependence was introduced by replacing the variable  $\Delta\beta/\beta$  with Poisson's ratio,  $\sigma$ . This was accomplished by taking the derivative of

$$\beta^2 = (.5 - \sigma)/(1 - \sigma) \alpha^2 \quad [22]$$

to yield

$$\Delta\beta/\beta \approx \Delta\alpha/\alpha - (1/4)[\Delta\sigma/(1 - \sigma)][1/(.5 - \sigma)]. \quad [23]$$

Replacing  $\Delta\beta/\beta$  in Aki and Richards's equation and employing a little bit of algebra, Shuey's equation is derived.

All the linear approximations in Fig. 3.D.7 are based on small variations in rock properties. The three classes of AVO defined by the models in Fig. 3.D.2 offer an excellent opportunity to validate the linear approximations for real-world environments. These approximations are illustrated in Fig. 3.D.8 along with the exact Zoeppritz solution.

While Shuey claimed that the linear-approximation equations were adequate to within a few degrees of the critical angle, this is not quite true. The three linear-approximation equations expressed in Fig. 3.D.7 yield almost identical results, except Bortfeld's is slightly more accurate for the large incident angles in the 4000-ft depth response. However, these angles are seldom of interest in conventional seismic.

All three equations are inaccurate for the 14,000-ft depth model, which has a large increase of velocity (dim out or Class 1 AVO anomaly). Fig. 3.D.8 contains AVO curves from the linear-approximation (red) and exact (black) equations out to 90° incident angles. Both the gas- and water-saturation models are plotted. The three linear-approximation equations yield results that overplot one another in Fig. 3.D.8.

The approximate solution for the wet case in the 14,000-ft model predicts an amplitude of zero at 30°, while the exact Zoeppritz solution predicts zero amplitude at the same incident angle for the gas case. As will be shown by an example later, the angle at which the reflection amplitude changes polarity is a diagnostic tool for evaluating Class 1 anomalies. Once again, the approximate solutions are not appropriate for Class 1 anomalies.

### *Shuey's Angle Dependence*

One of Shuey's main contributions is that he identified how various rock properties can be associated with near-, mid-, and far-angle ranges. On the right side of Shuey's equation in Fig. 3.D.7, the first term is the normal-incident reflectivity and this is constant across all incident angles. The second term does not start to contribute significantly until incident angles of 15° or greater are reached. The third term, Shuey argued, is

insignificant and can be ignored if the incident-angle range is beneath  $30^\circ$ . Using only the first two terms of his equation, Shuey illustrated that Koefoed's conclusions were easy to verify. Shuey, like Koefoed, didn't offer any petrophysical evidence that Poisson's ratio was directly related to lithology. However, he did provide the incentive for the industry to use only the zero-offset and mid-angle contributions to the reflection-coefficient equation to extract estimates of Poisson's ratio. He showed how both the normal-incident coefficient,  $NI$ , and the change in Poisson's ratio,  $\Delta\sigma$ , could easily be extracted from the amplitudes in a CDP gather. Having the ability to extract these two parameters, Shuey continued by suggesting that the rock properties in an area be crossplotted in terms of  $\ln(\rho\alpha)$  versus Poisson's ratio,  $\sigma$ . Now with the extracted  $NI$  and  $\Delta\sigma$  from seismic and the crossplot from well-log data, an estimate of the lithology could be made. This was the first practical method suggested for extracting lithology from seismic data. Ostrander verified Koefoed's prediction, and Shuey showed how to implement Koefoed's theory. This was a major contribution to the AVO attribute era.

Both the first and second term in Shuey's equation contain the normal-incident reflection coefficient,  $NI$ . Verm and Hilterman (1995) rearranged Shuey's equation to emphasize the rock-property dependence on incident angle as illustrated in Fig. 3.D.9. With this new arrangement, the near-angle response is basically influenced by changes in acoustic impedance; the mid-angle response is influenced by variations in Poisson's ratio; and, the far-angle, by variations in  $P$ -wave velocity. Of course, there must be a variation in an individual rock-property for the contributions in a particular angle range to respond. The AVO response from this equation is the same as Shuey's original form and also Aki and Richards's.

Synthetic AVO responses (Fig. 3.D.10) were generated for each of the three rock-property terms. The left panel was generated from the first term in Fig. 3.D.9, and the main rock property contributing to this response is the acoustic impedance. The second-term response is displayed in the middle panel. This panel responds to changes in Poisson's ratio. The right panel, which is the large incident-angle response, has insignificant energy for this example.

It is interesting to note that the AVO response from Poisson's ratio is not always in phase with the acoustic-impedance contribution. Also, where there are large contributions from acoustic impedance, the Poisson's ratio contribution can be rather small, and vice versa. The question remains, "How does this relate to lithology?"

Fig. 3.D.11 is a repeat of the center panel of Fig. 3.D.10 with the well-log curves displayed next to the AVO response. The AVO response, is the Poisson's ratio contribution. The velocity and density curves are plotted to the left of the Poisson's ratio AVO response, while the resistivity curve is plotted to the right. The geology consists mainly of unconsolidated sands and shales. The resistivity curve depicts sand beds as deflections to the left (low-resistivity values). The strong correlation between the Poisson's ratio AVO response and the sand beds suggests that if Poisson's ratio can be extracted from the seismic data, an excellent sand-versus-shale discriminator would exist. This would be a lithologic AVO attribute.

There is a disclaimer that must be acknowledged for this comparison. In order to compute the AVO response, either a measured  $S$ -wave velocity curve is needed, or an estimate of it. For the comparison in Fig. 3.D.11, the  $S$ -wave curve was estimated using

the Greenberg-Castagna and Batzle-Wang techniques that were described in the petrophysical section. To some extent, the conclusion might be considered biased. However, comparisons of S-wave log estimates versus logged dipole sonics in the same area have shown excellent correlations.

### *Modeling: Exact Versus Approximate Solutions*

Several times it was mentioned that the linear-approximation equations are inadequate for large velocity contrasts, especially for high-velocity beds encased in low-velocity formations. Anomalous high-amplitude responses on the large offsets exist. The AVO response in Fig. 3.D.12 has two high-amplitude events annotated. When the sonic and Poisson's ratio curves are examined, there are no beds thick enough, with large rock-property contrasts, to warrant these high amplitudes on the far-offset traces.

In the computation of this AVO response, the well-log curves were depth sampled in units equivalent to 1-ms time intervals. That corresponds to sampling the depth log at approximately 5-ft intervals. This might be considered oversampling. The exact Zoeppritz solution was then employed. AVO synthetics were also generated for the same model using the linear-approximation solution and the total elastic solution. The same input logs were used for the linear-approximation, exact Zoeppritz, and total elastic solutions. The resulting AVO responses are shown in Fig. 3.D.13.

The total elastic solution contains all multiples, converted events, direct arrivals, head waves, etc. It is considered to be the true solution. Its response is displayed in the upper-right corner next to the ray-trace exact Zoeppritz solution with *PP* waves only. The total elastic AVO response does not exhibit the large amplitudes on the far traces. The Zoeppritz solution has inaccurate amplitudes on the far traces when applied to logs that were depth sampled equivalent to 1-ms time intervals. The linear-approximation solution for the same model is displayed in the lower-right corner. Its AVO response closely matches the total elastic model. However, when a coarser depth sampling interval (equivalent to 4-ms time sampling) is utilized on the initial well-log curves and the exact Zoeppritz solution is applied, the AVO response more closely matches the total elastic model. At first, this doesn't appear to be logical.

The model in Fig. 3.D.14 will assist in describing these inconsistencies. A 13,000 ft/s bed is encased between 9000 ft/s formations. The exact and linear-approximation amplitude versus incident-angle curves are plotted for both the upper and lower interface. If the incident angle is  $30^\circ$ , the refracted angle is  $46^\circ$ . For the top interface, the point labeled ET (a value of 0.16) indicates the exact Zoeppritz reflection coefficient. For the bottom interface, the exact Zoeppritz reflection coefficient is indicated by EB ( $-0.06$ ). When the thickness of the bed approaches zero, the refracted angle does not change significantly. Thus, an amplitude of 0.16 will be added to  $-0.06$  at the same time arrival (bed thickness  $\Rightarrow$  zero), leaving a residual amplitude of 0.10. This is the source of the anomalous far-offset anomaly when only *PP* waves are considered.

For the linear approximation, the incident and refracted angles are averaged. For a  $30^\circ$  incident angle, the computations use  $(30^\circ + 46^\circ)/2 = 38^\circ$ . Likewise, when the incident angle is  $46^\circ$  for the bottom interface, the computations use  $38^\circ$ . Thus, it is not surprising that the reflection coefficient for the upper interface at  $30^\circ$  incident for the linear solution, ST, has the same magnitude as the bottom-interface reflection coefficient at



46° incident (SB). The sign of the amplitude curves are opposite. In short, as the thin bed approaches zero thickness, the linear-approximation solution approaches zero amplitude. The exact Zoeppritz solution with only *PP* waves included does not. Simmons and Backus (1994) noted this false anomalous amplitude for beds with large velocity contrasts. This effect is more pronounced though for high-velocity beds than low-velocity beds.

When the sampling for the input model is coarser (depth equivalent of 4 ms), the thin bed has its high-velocity values averaged with the surrounding low-velocity formations. Thus, the velocity contrast reduces and the problem solves itself—not a perfect solution, but one to try when high-velocity beds are encountered. In summary, don't use the exact Zoeppritz solution when high-velocity beds are encountered; a total elastic solution is necessary.

### 3E. Linear-Approximation Equation with Anisotropy

#### *Properties of Anisotropic Media*

An anisotropic rock has variations in its physical properties that depend upon the direction a property is measured. In a rock with a north-south fracture system, permeability measurements in that direction are larger than measurements in the east-west direction. Likewise, in the same rock, a *P*-wave propagating in the north-south direction has a faster velocity than one traveling in the east-west direction. However, the *S*-wave velocity in the east-west direction will be larger. This type of anisotropy is called horizontal transverse isotropy or HTI (Fig. 3.E.1).

Another anisotropic model, which is more commonly considered, is vertical transverse isotropy (VTI). Alternating thin layers that are individually isotropic but have significantly different *P*-wave velocities can induce VTI. For horizontal layering, seismic waves normally travel faster in the horizontal direction than in the vertical. This is the principal reason that depth estimates based on seismic-velocity analyses are too deep; the *rms* velocity derived from stacking analyses measures the horizontal-component of velocity and not the vertical.

A few wave-propagation effects of VTI models that will have an impact on amplitude interpretation are diagrammed in Fig. 3.E.2. The fact that the incident phase angle in an anisotropic medium is different from that in an isotropic medium influences an amplitude interpretation. For VTI media, this incident-angle difference becomes significant around 40° to 50°.

While the VTI model discussed above can be thought of as a macroscopic effect, VTI effects also exist in individual layers. Shale, because of its intrinsic nature of having a platy structure, tends to be stronger in the horizontal direction than in the vertical. Once again, the horizontal velocity is faster than the vertical velocity.

Accounting for anisotropic effects in the seismic method was greatly advanced by the pioneering work of Thomsen in 1986. Thomsen simplified the tedious math that is normally associated with anisotropic wave propagation. Two of his weak anisotropic parameters ( $\epsilon$  and  $\delta$ ) are related to the wave-propagation effects mentioned, and these are defined in Fig. 3.E.3. Thomsen's third parameter, which is not discussed here, is

related to S-wave propagation. The last term in Fig. 3.E.3,  $\eta$ , is dependent on Thomsen's first two parameters, and it is this term ( $\eta$ ) that relates to NMO velocity measurements (Fig. 3.E.4).

### Measurement and Application

Alkhalifah and Tsvankin (1995) published the NMO equation for anisotropic media (Fig. 3.E.4). Numerous articles authored by Tsvankin around this same time period dealt with other practical applications of anisotropy. Tsvankin and Thomsen (1994, 1995) jointly authored two of these papers. The significance of Tsvankin's work on anisotropy won him the SEG Virgil Kauffman Gold Medal in 1996.

In order to estimate Thomsen's anisotropic parameters,  $\epsilon$  and  $\delta$ , from seismic data, additional information at a well location is needed. The estimation procedures are roughly illustrated in Fig. 3.E.4. During a velocity analysis using the illustrated equation, two unknowns are required,  $V_{NMO,SS}$  and  $\eta$ , at each two-way time,  $t_0$ .  $V_{NMO,SS}$  is the short-spread velocity analysis performed by initially muting the CDP gather to offset = depth. After  $V_{NMO,SS}$  is estimated, the unmuted CDP gathers are scanned for  $\eta(t_0)$ . Finally, adjustments to  $V_{NMO,SS}$  and  $\eta(t_0)$  are performed.  $\eta(t_0)$  can be estimated only if energy is on the far-offset traces. Therefore, for any CDP gather, there are more velocity picks than  $\eta$  picks.  $\eta(t_0)$ , derived from the velocity analysis, is an "rms" function that must be reduced to individual layer values for subsequent modeling. Once this is done, layer values for  $\delta$  and  $\epsilon$  can be computed as indicated in the figure. Can these layer estimates of  $\delta$  and  $\epsilon$  be used to study the anisotropic effect during an amplitude interpretation? Unfortunately, the time resolutions of these  $\delta$  and  $\epsilon$  estimates are normally too coarse to assign anisotropic values to media above and below the reflection of interest. This is not a desirable situation because of the potential anisotropic effect on the reflection amplitude.

The contribution of anisotropy can be added to the isotropic linear-approximation equation as illustrated in Fig. 3.E.5. This anisotropic approximation, along with equations for other anisotropic models such as HTI, can be found in Ruger's PhD thesis (1996).

In Fig. 3.E.5, typically measured values for  $\delta$  and  $\epsilon$  were assigned only to the shale properties for the 9000-ft (3000-m) depth model (Fig. 3.D.2). The decision to assign anisotropy only to shale has been questioned by several authors. AVO responses were generated for the wet- and gas-saturated states. There are significant differences between the AVO responses with and without anisotropy. With the current trend of applying nonhyperbolic NMO corrections, the amplitude variations beyond  $40^\circ$  need to be reconciled by the interpreter. Are observed large amplitudes on the far-offset traces caused by lithologic, pore-fluid, or anisotropic variations? Recently, Bork et al. (1997) concluded that the unusual AVO anomalies they were observing in the Gulf of Mexico and Trinidad were directly related to VTI anisotropy. However, they also noted that much research is still necessary to make this a viable exploration tool.

## Figures

Figure 3.A.1

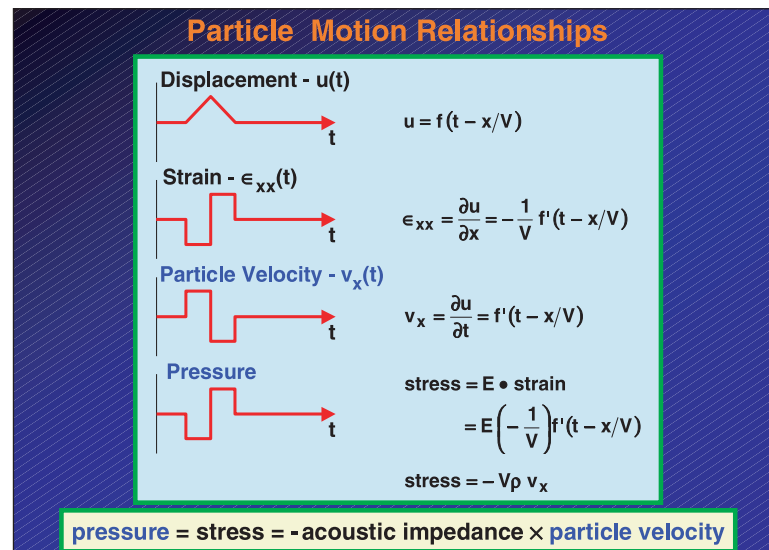


Figure 3.A.2

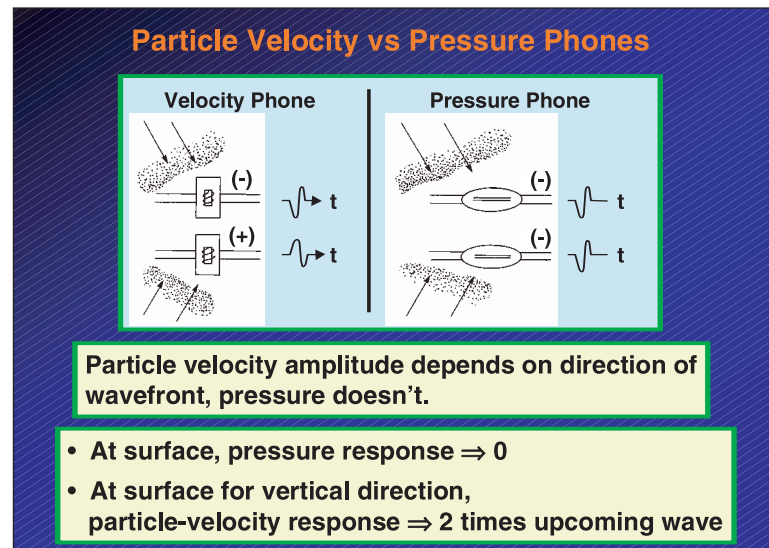


Figure 3.A.3

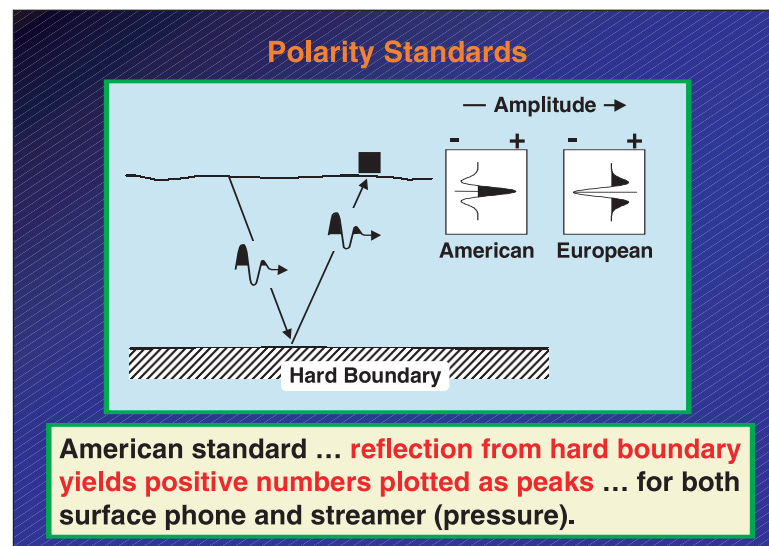


Figure 3.A.4

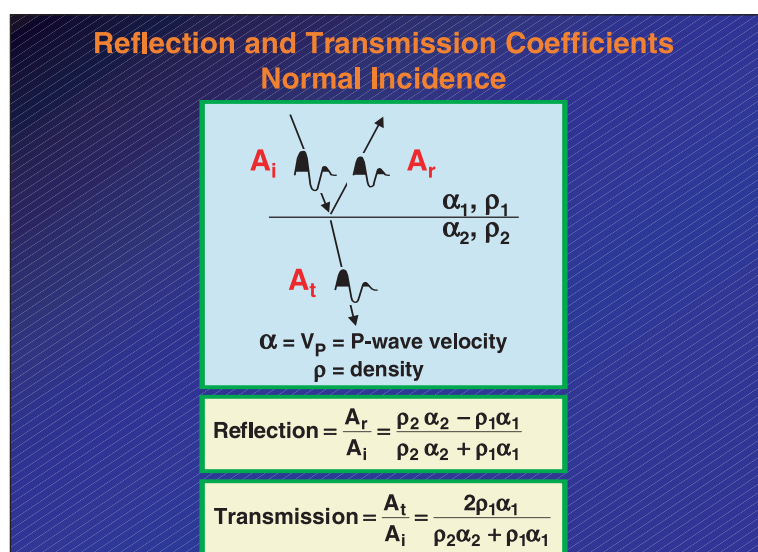


Figure 3.A.5

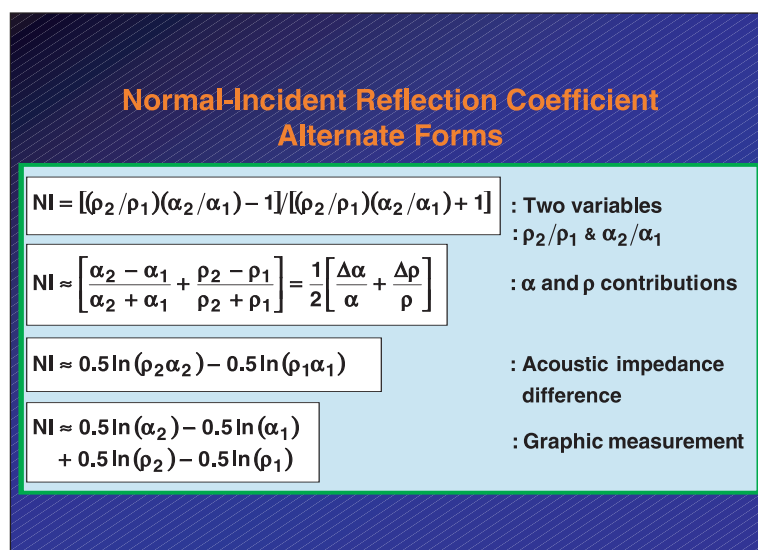


Figure 3.A.6

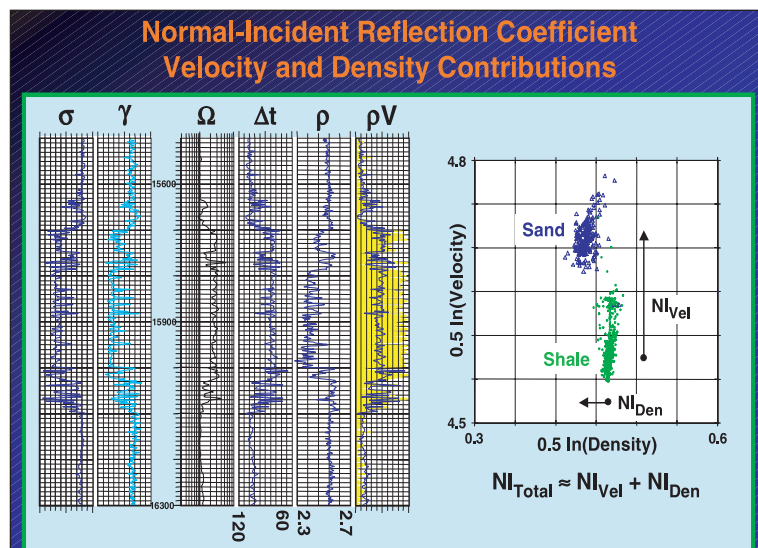


Figure 3.B.1

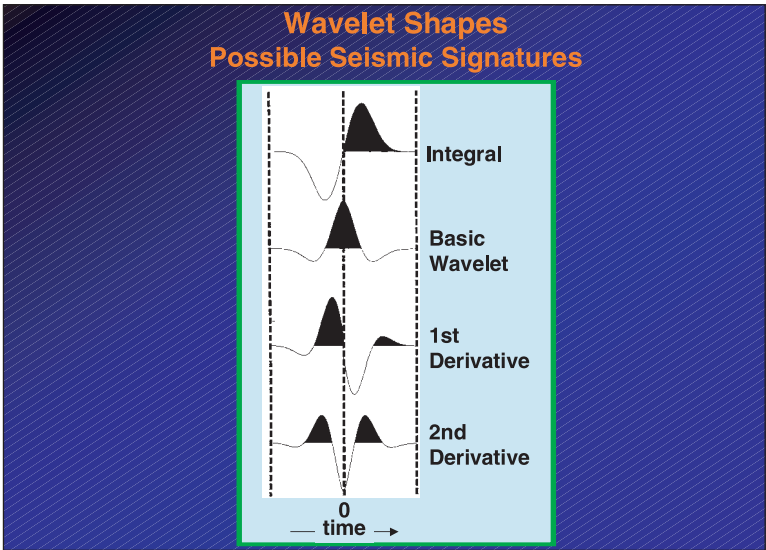
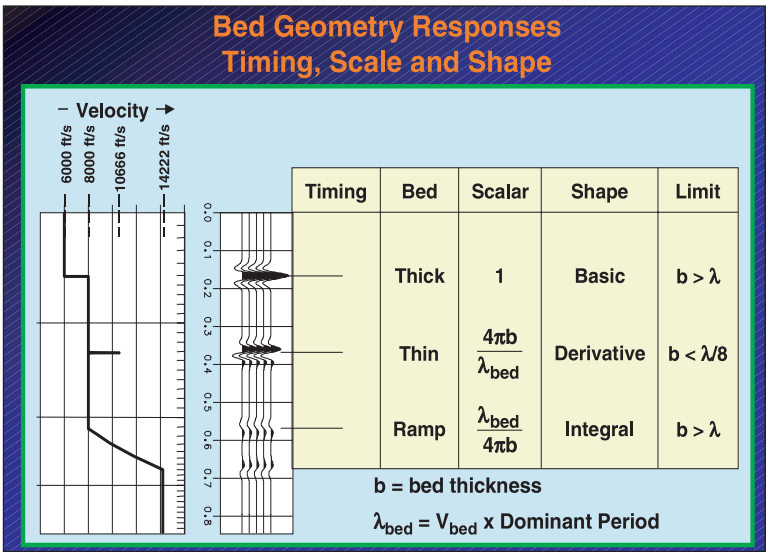


Figure 3.B.2





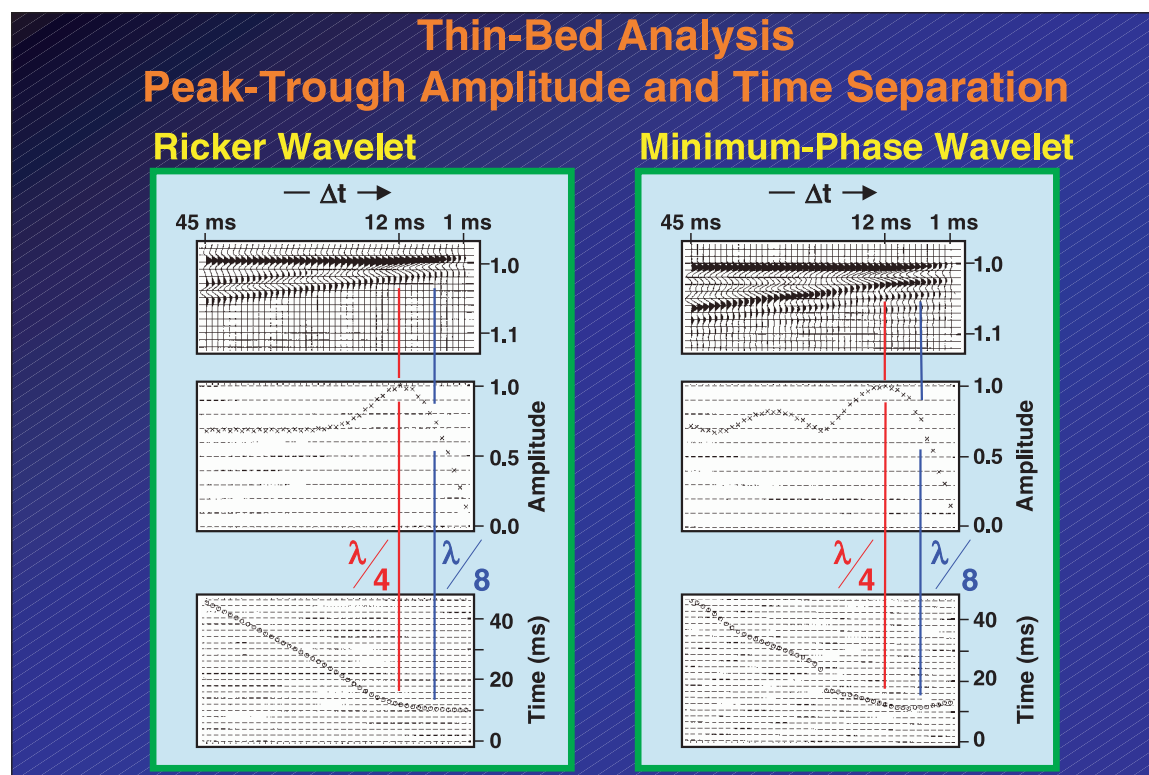


Figure 3.B.3

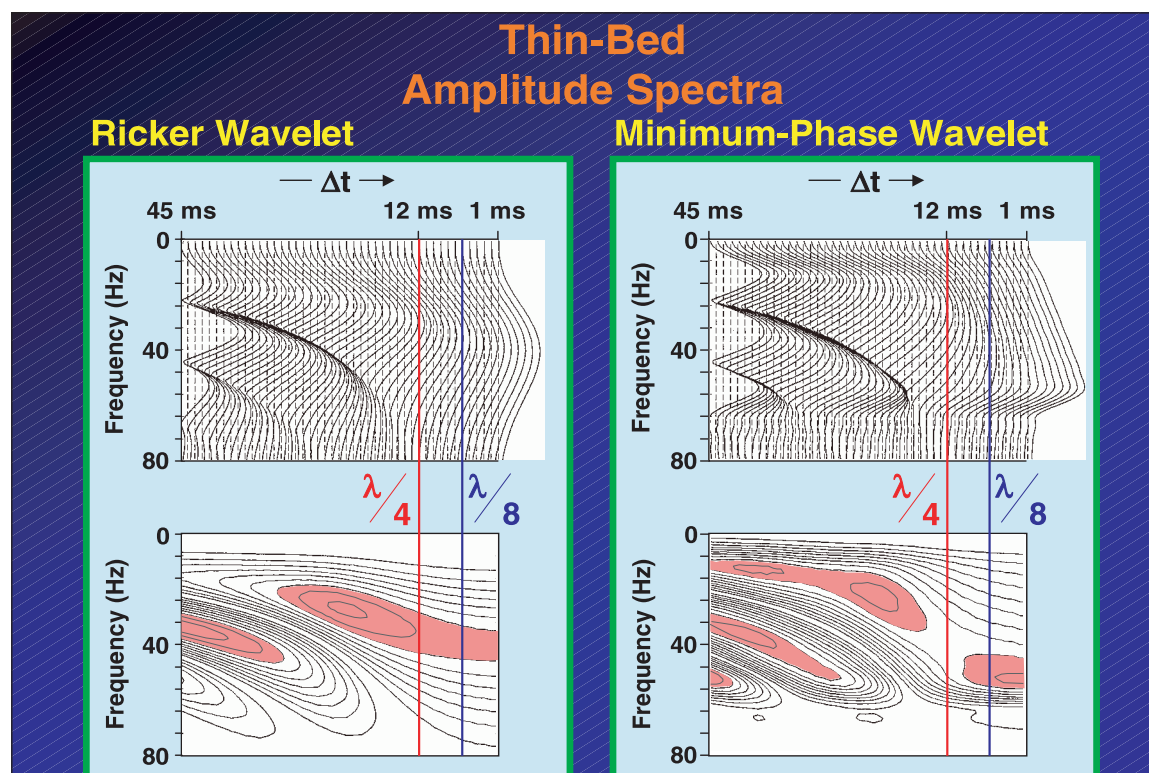


Figure 3.B.4

Figure 3.B.5

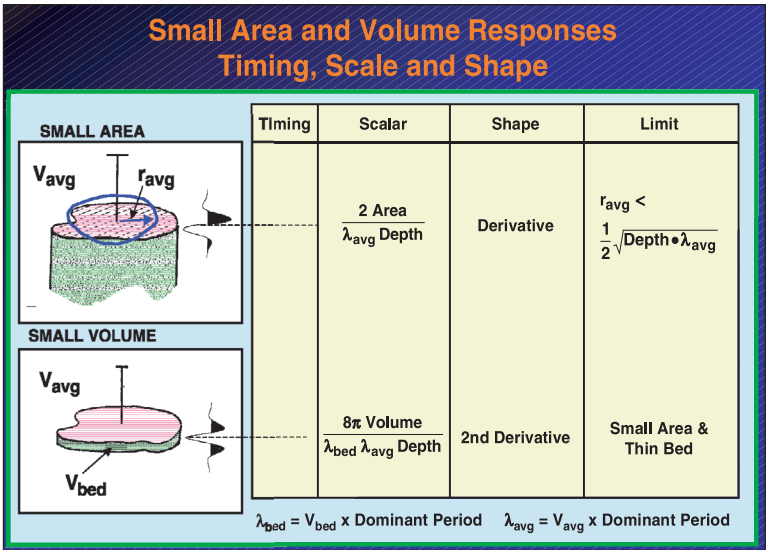
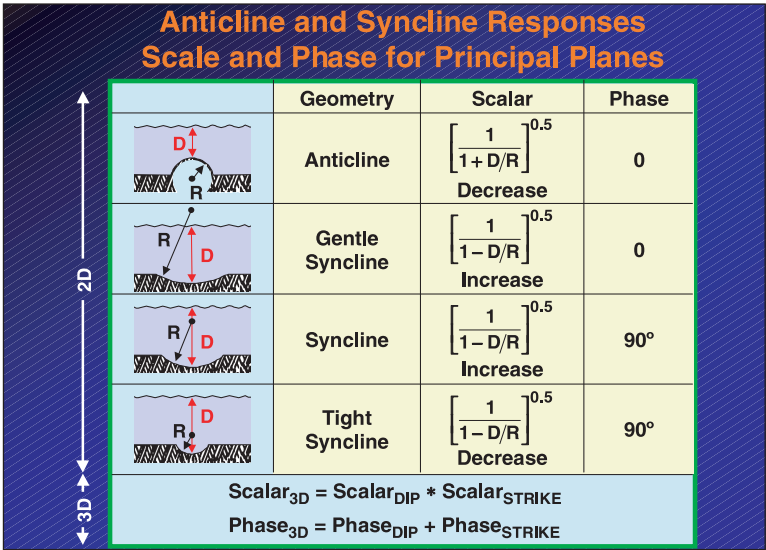


Figure 3.B.6



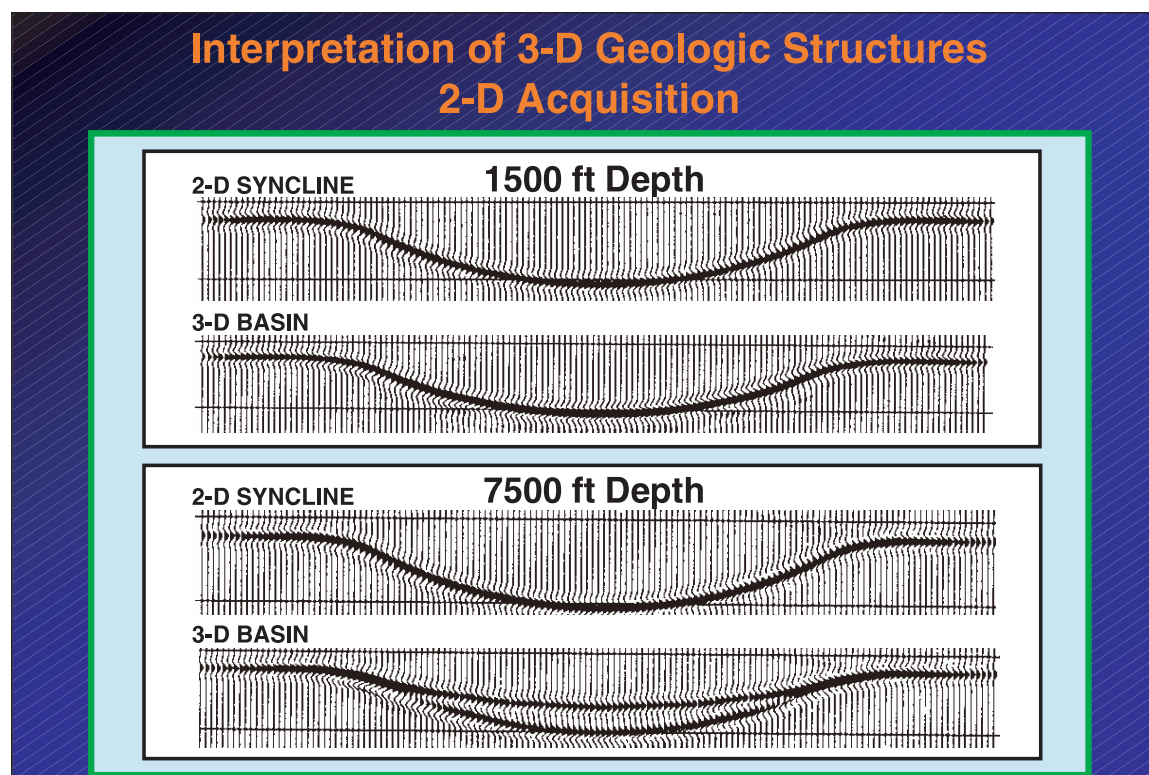


Figure 3.B.7

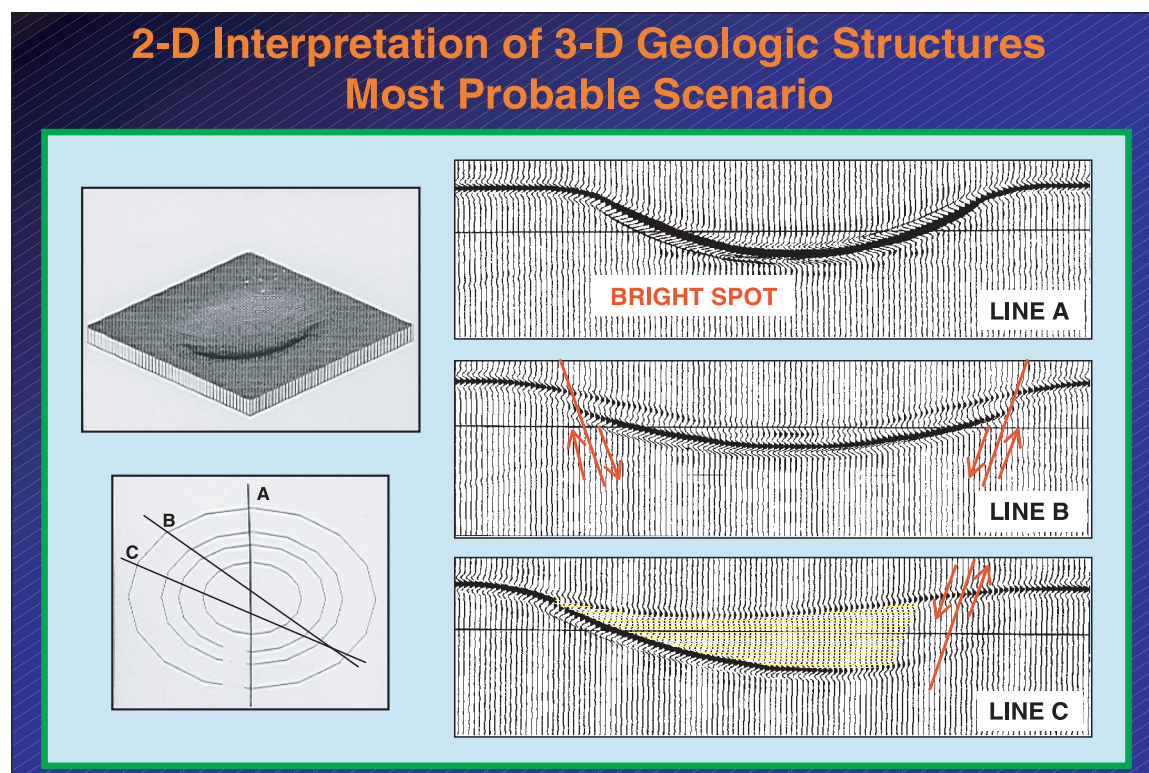


Figure 3.B.8

Figure 3.B.9

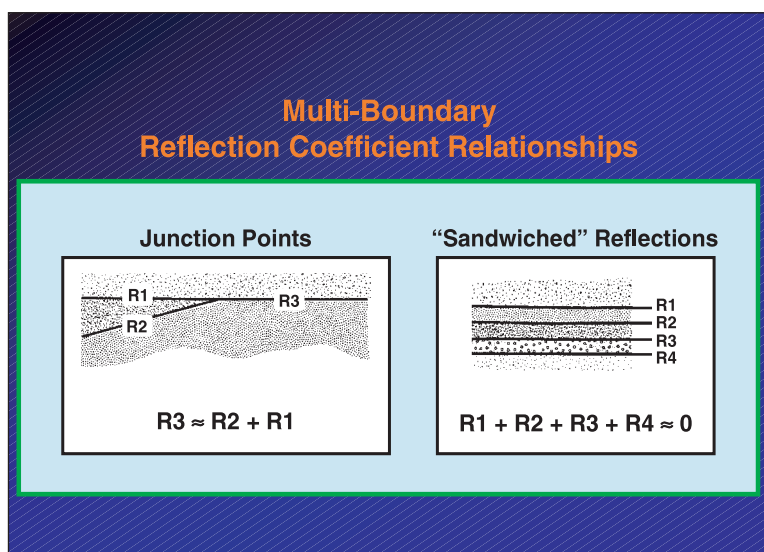


Figure 3.C.1

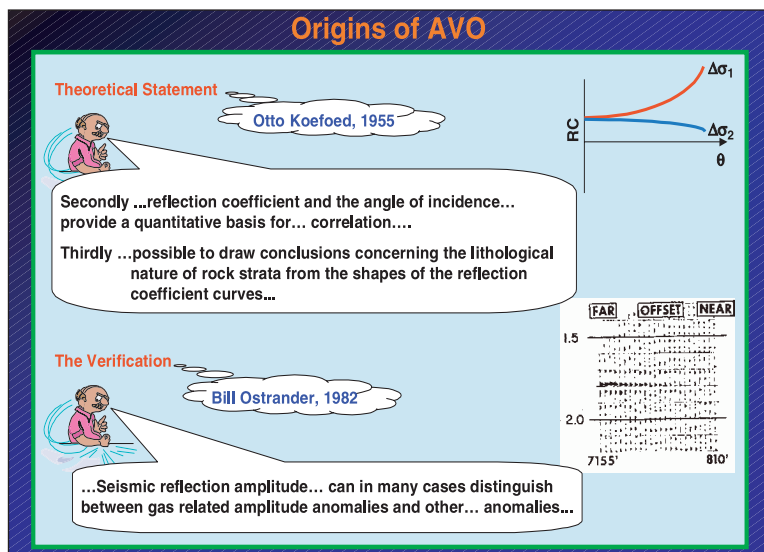


Figure 3.C.2

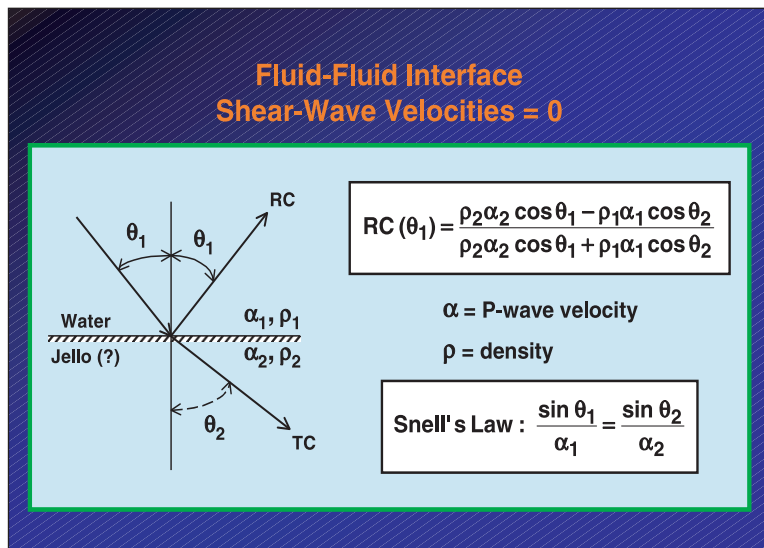


Figure 3.C.3

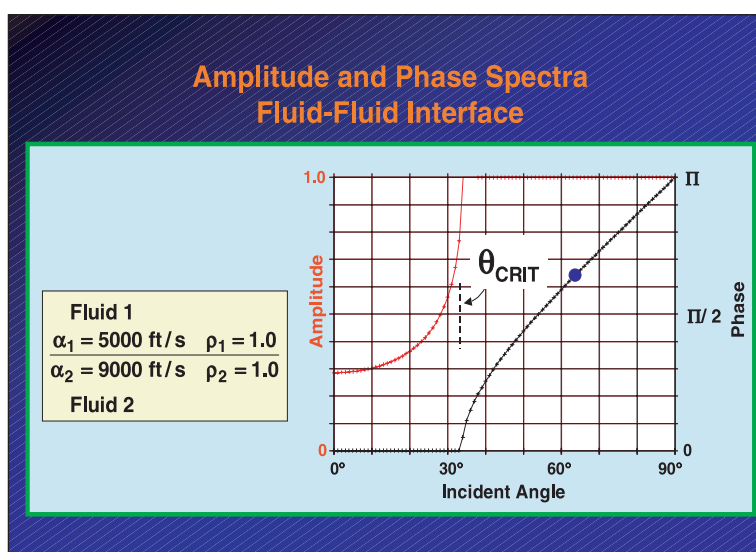


Figure 3.C.4

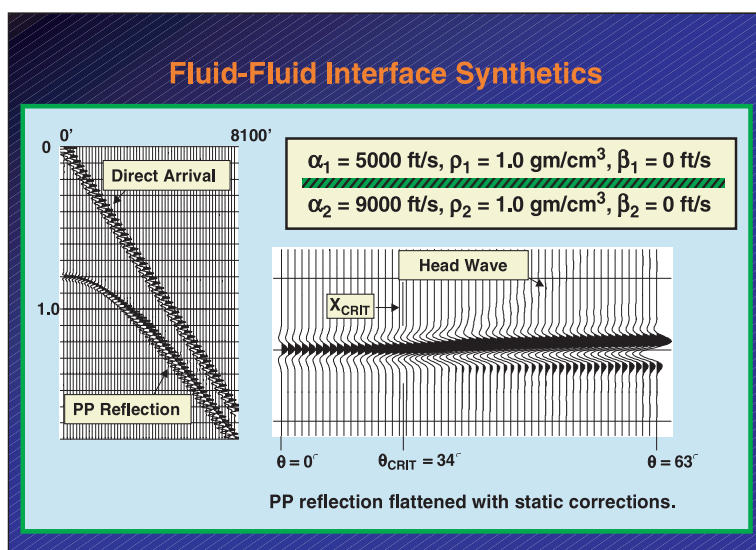


Figure 3.C.5

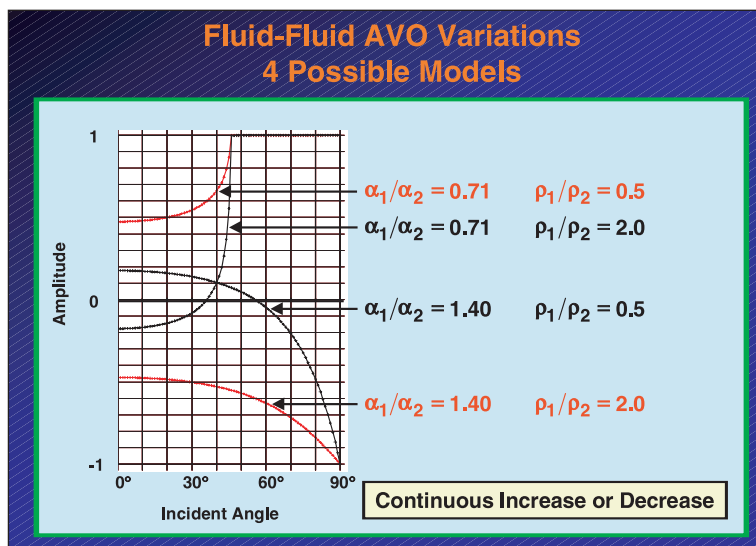




Figure 3.C.6

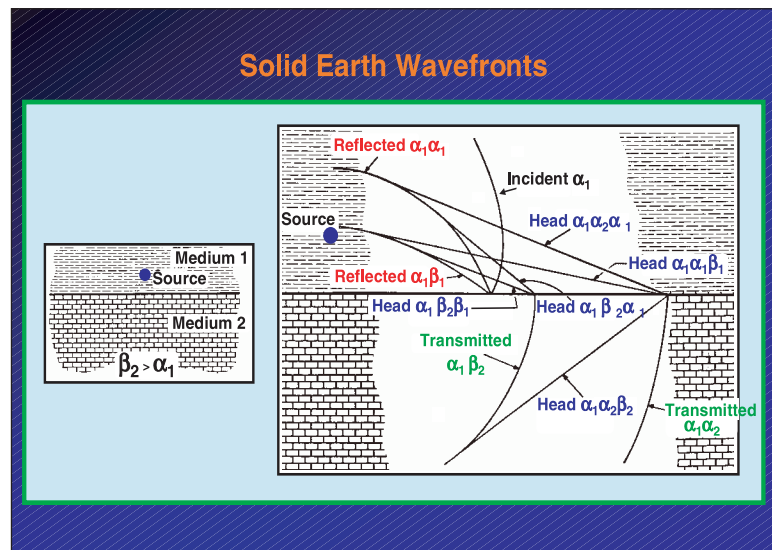


Figure 3.C.7

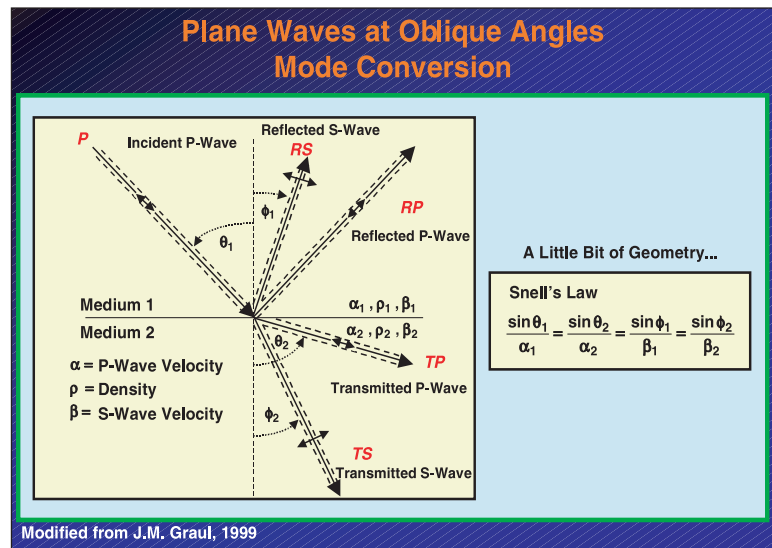


Figure 3.C.8

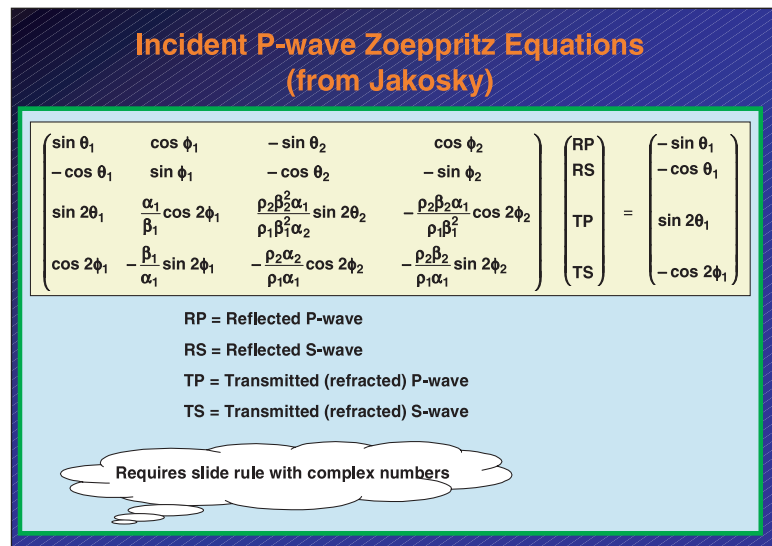


Figure 3.C.9

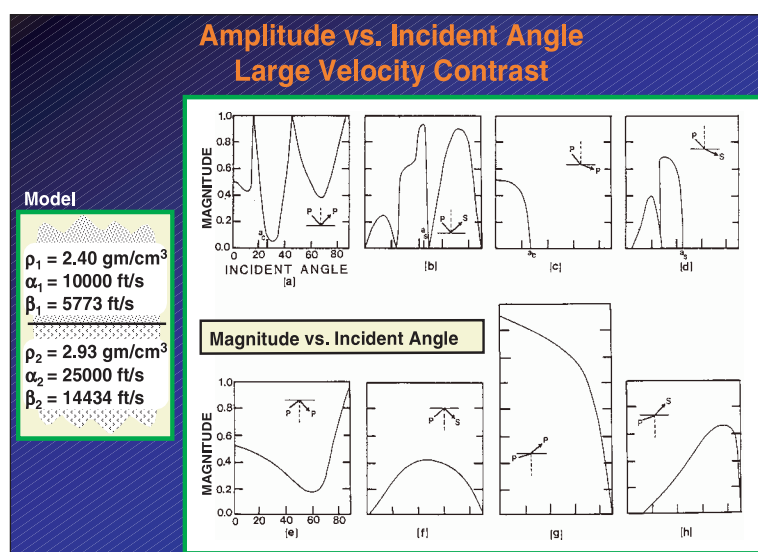


Figure 3.C.10

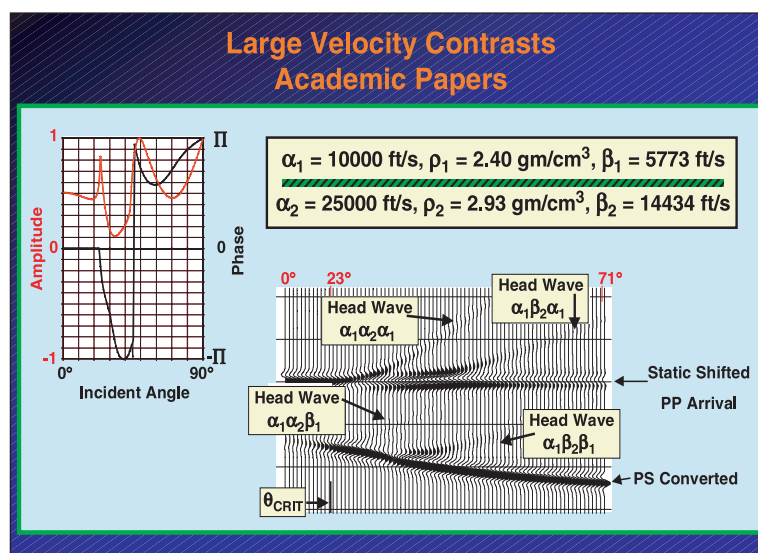


Figure 3.C.11

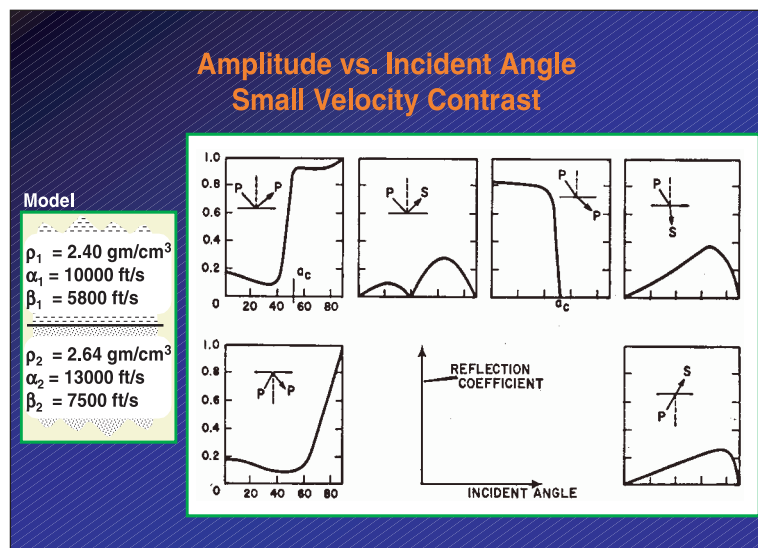


Figure 3.C.12

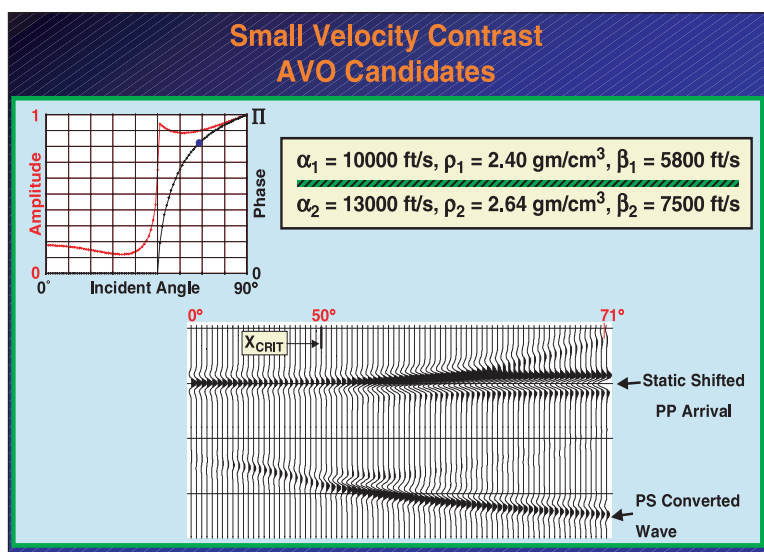


Figure 3.C.13

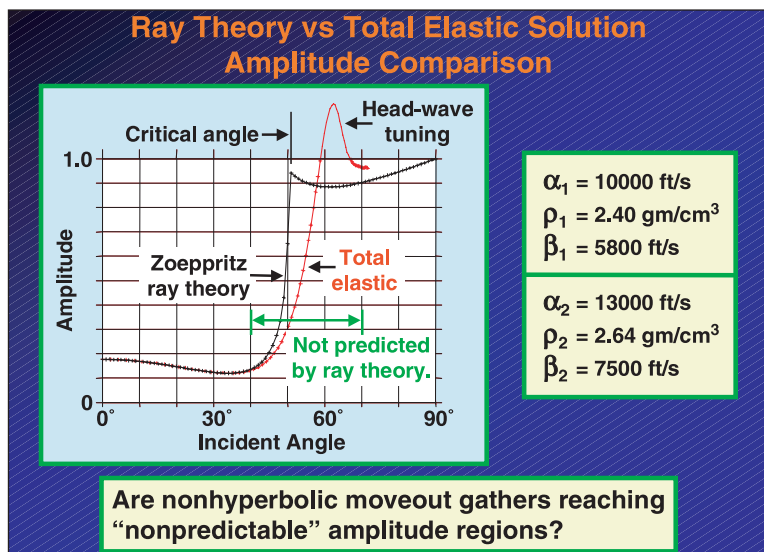
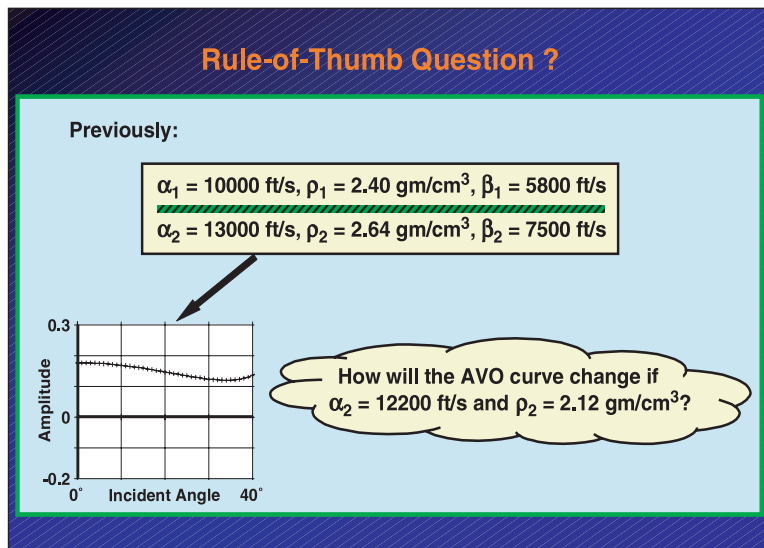


Figure 3.C.14



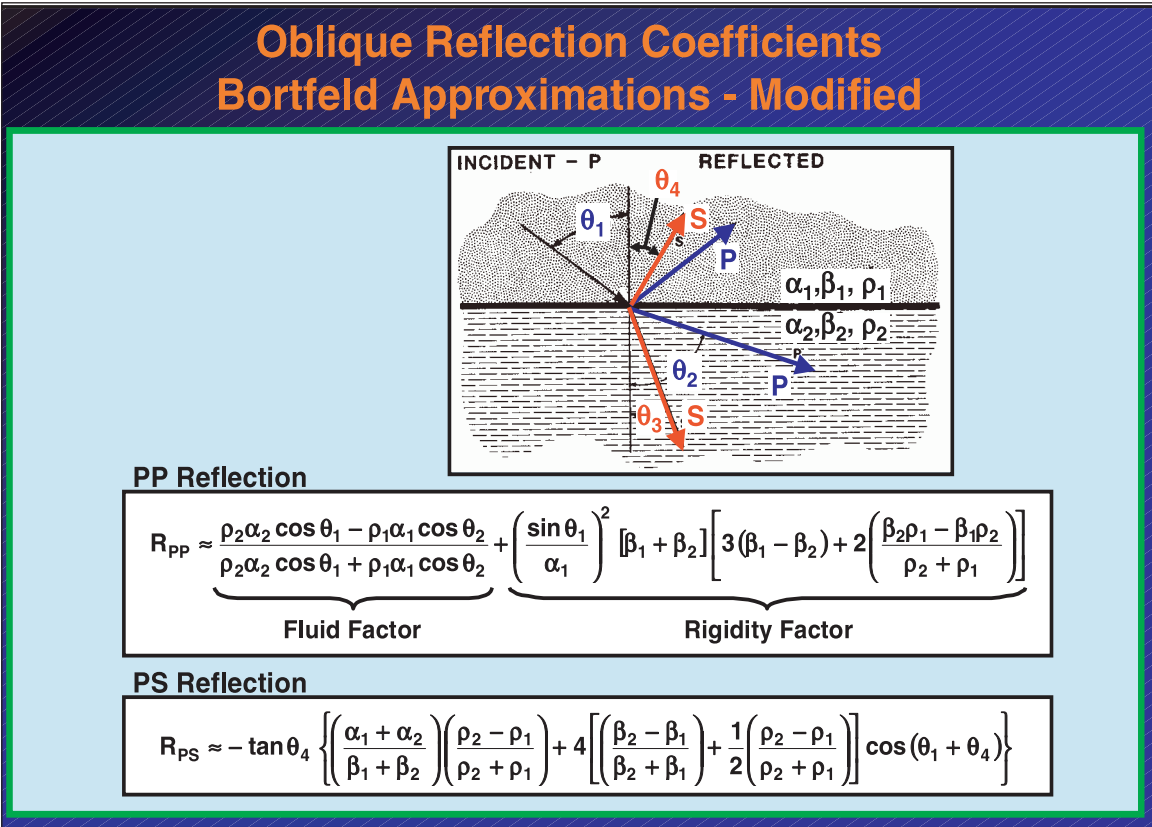
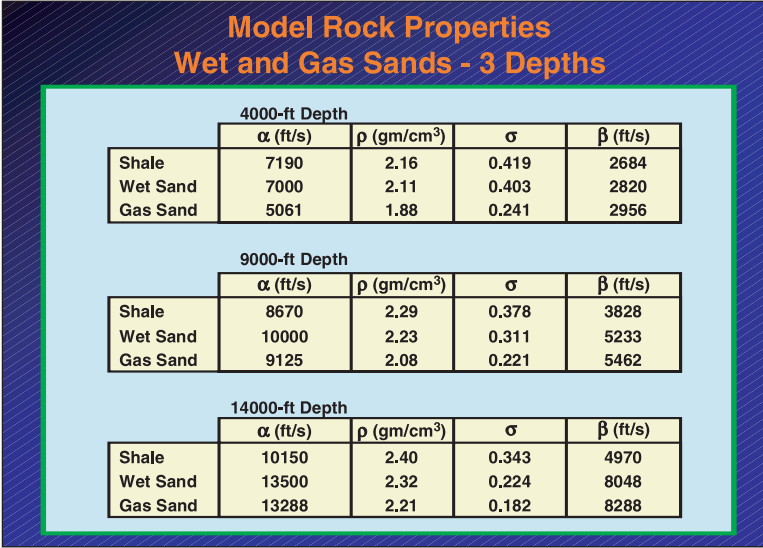
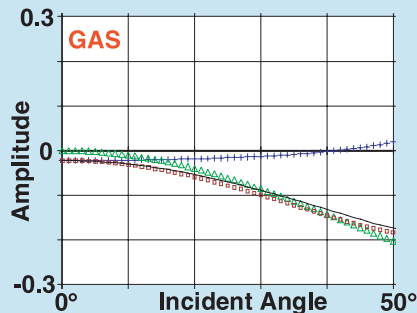
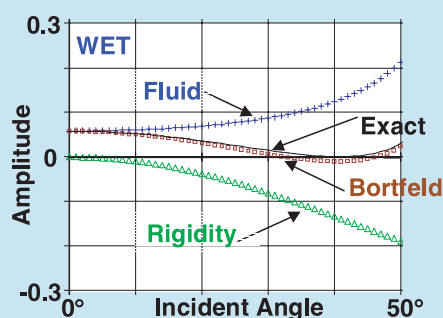


Figure 3.D.1

Figure 3.D.2



## Pore-Fluid Prediction by Bortfeld Sand at 9000-ft Depth

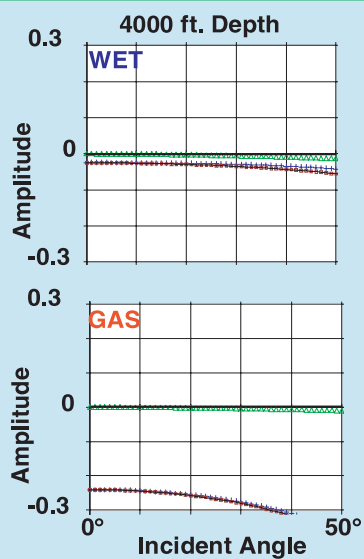


- Rigidity response is same for wet and gas models.
- Fluid term identifies pore-fluid content.

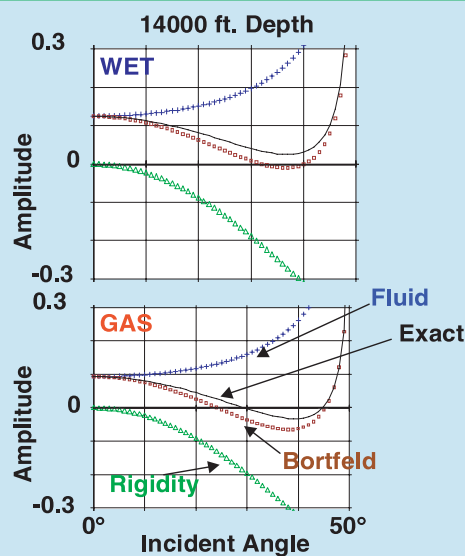
Rigidity term function of lithology ?

Figure 3.D.3

## Bortfeld Responses Shallow & Deep Gas Sands



$$(\text{Rigidity})_{\text{GAS}} \approx (\text{Rigidity})_{\text{WET}}$$



Shallow: Small slope for rigidity term

Deep: "Bortfeld" approximation not accurate

Figure 3.D.4

Figure 3.D.5

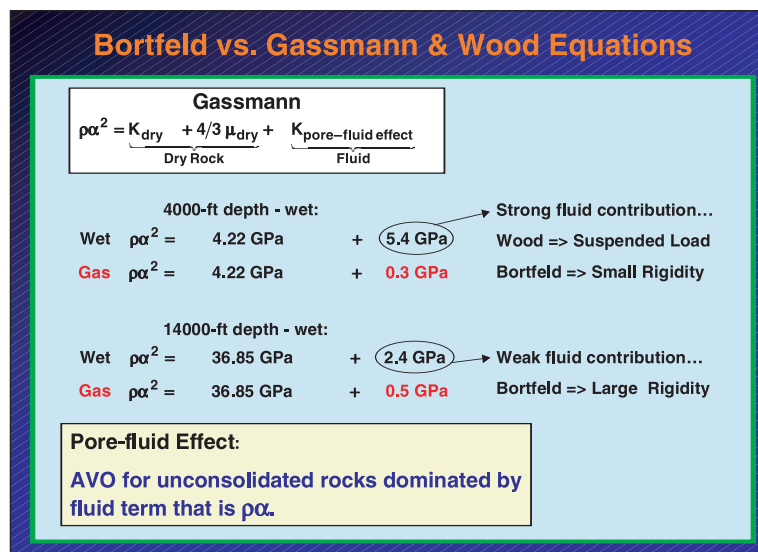


Figure 3.D.6

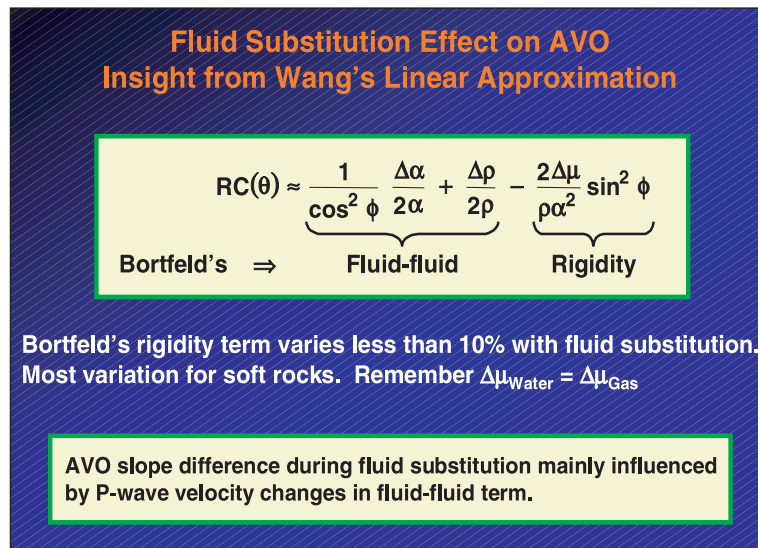
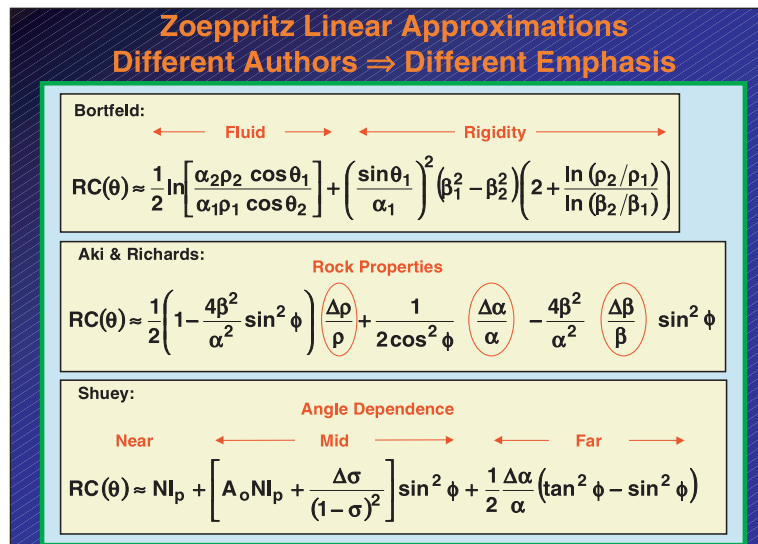
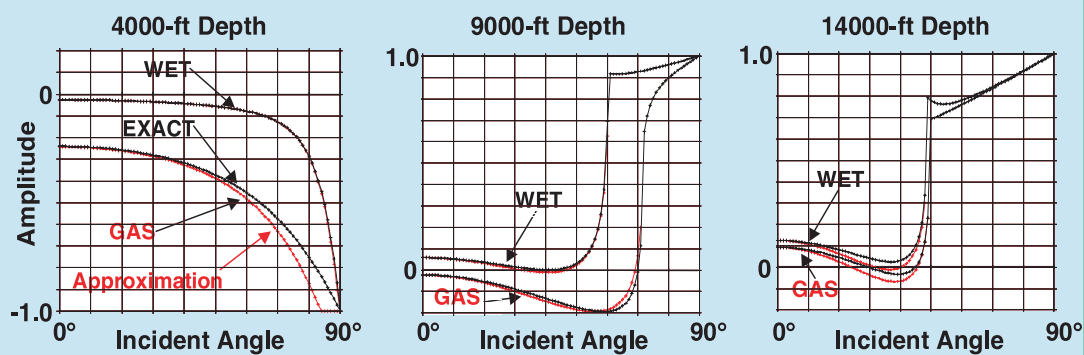


Figure 3.D.7





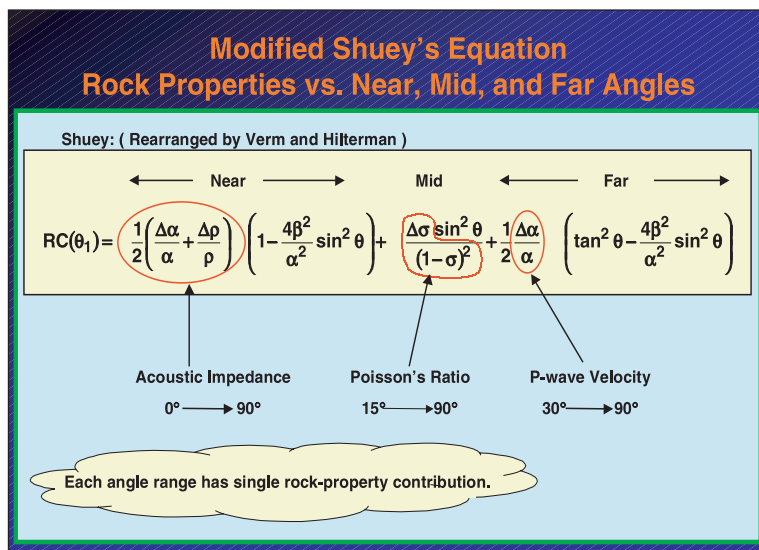
## Accuracy of Linear Approximations Bortfeld, Shuey, Aki & Richards



- Shuey = Aki & Richards  $\approx$  Bortfeld
- Bortfeld slightly more accurate for unconsolidated rocks.
- All approximations have problems with consolidated rocks.

Figure 3.D.8

Figure 3.D.9



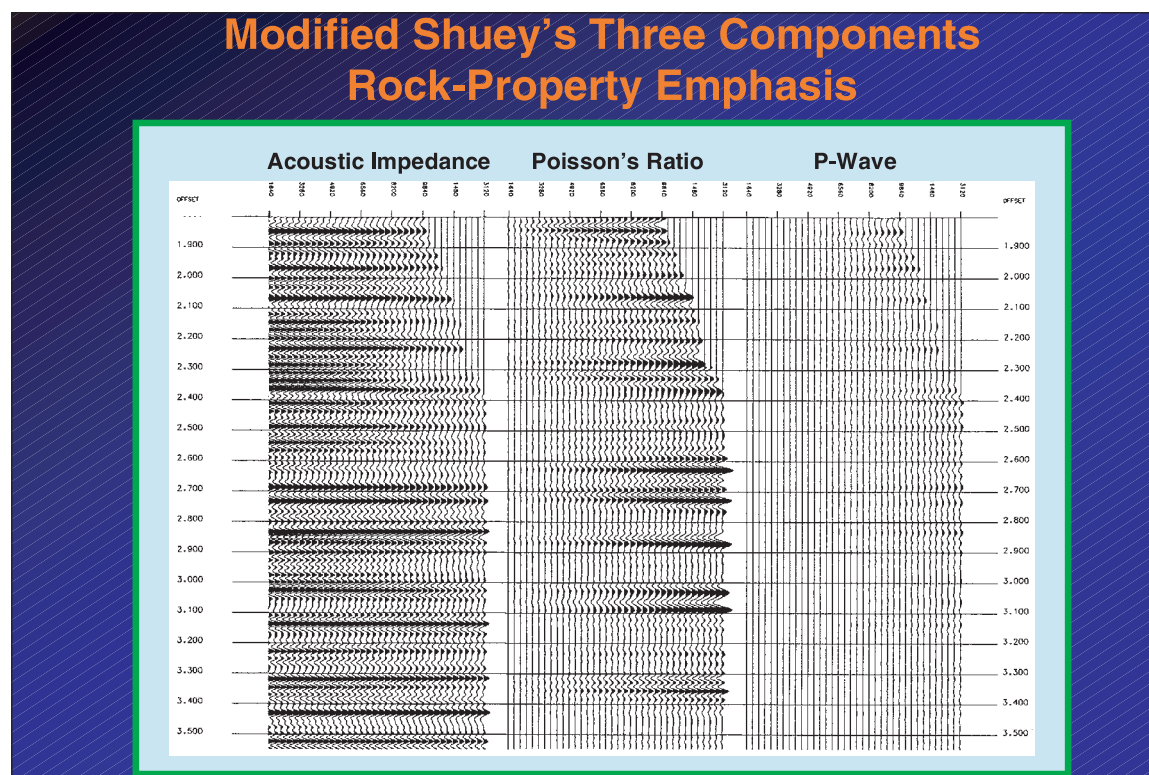


Figure 3.D.10

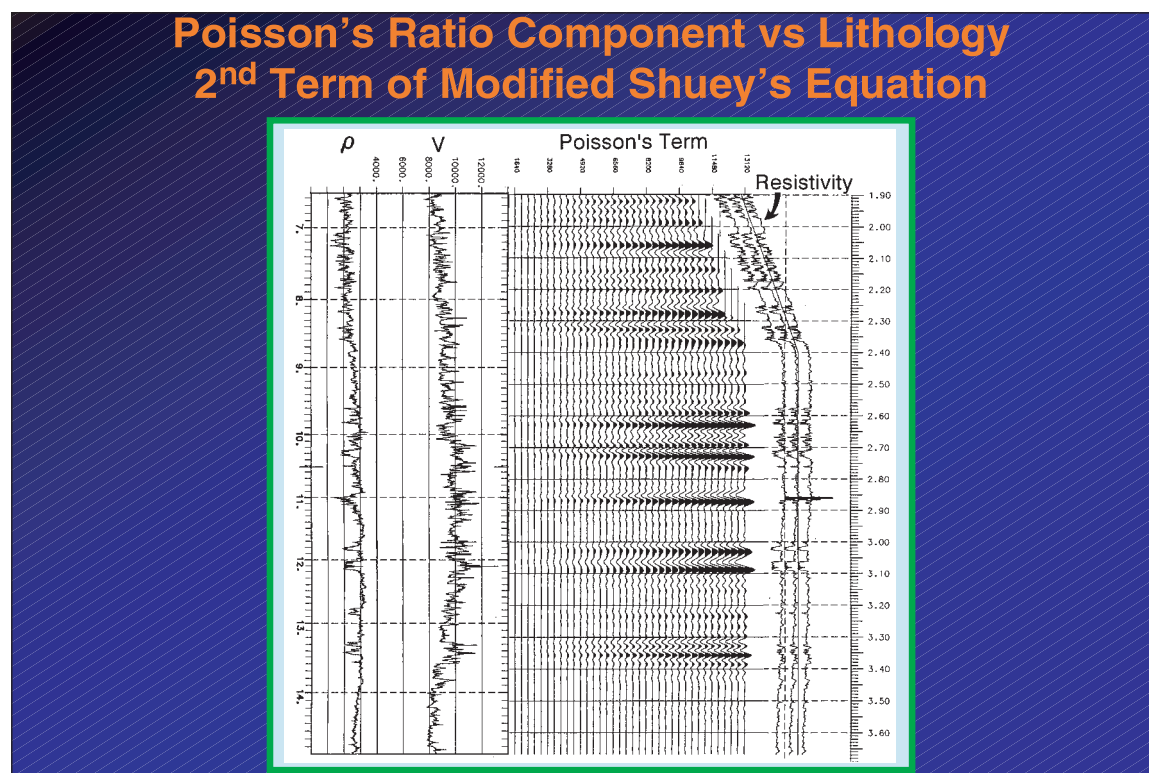


Figure 3.D.11

Figure 3.D.12

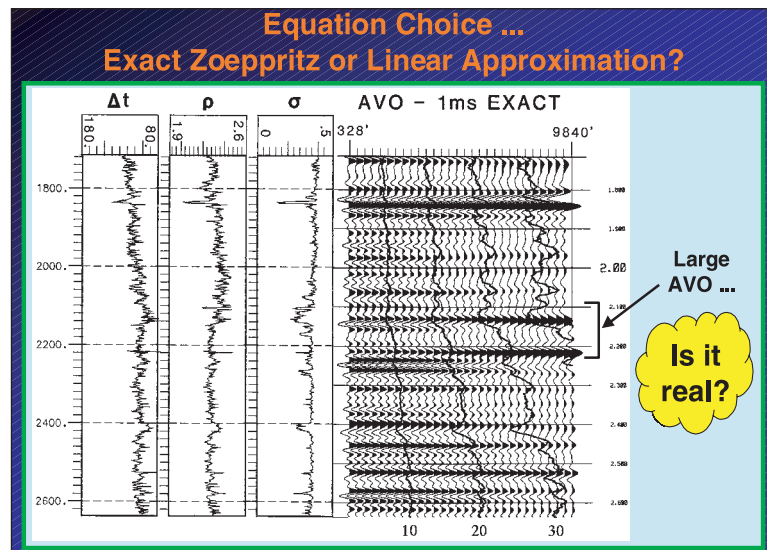


Figure 3.D.13

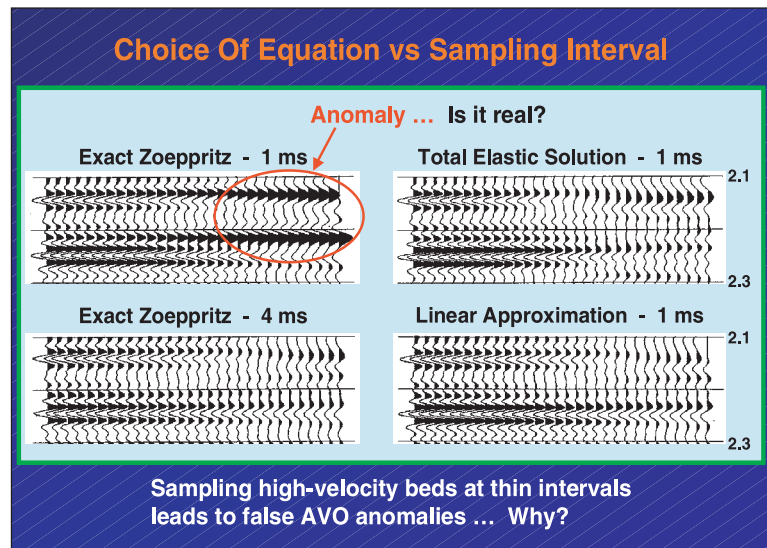


Figure 3.D.14

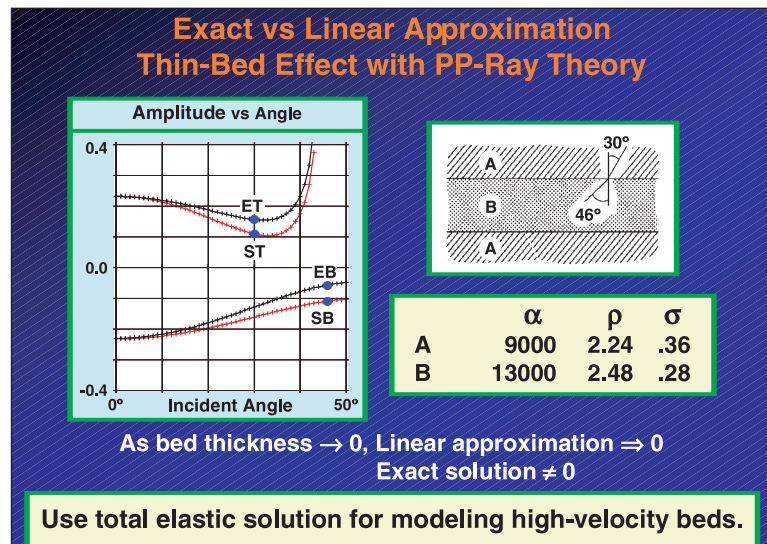


Figure 3.E.1

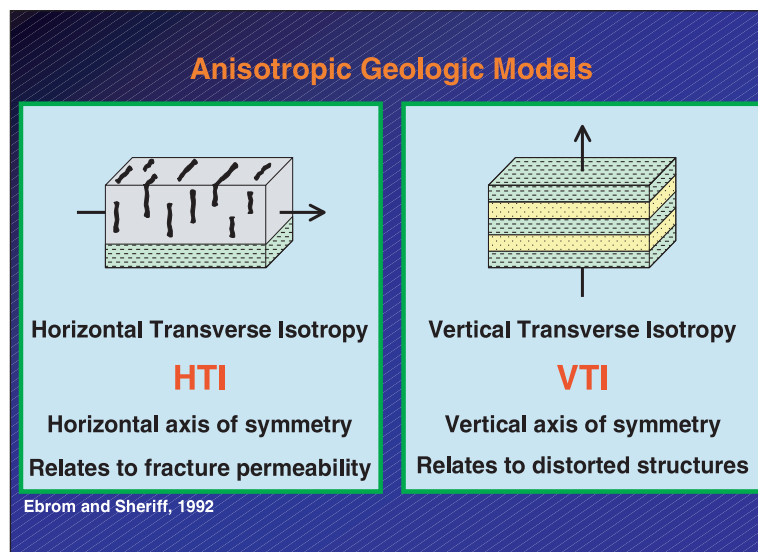


Figure 3.E.2

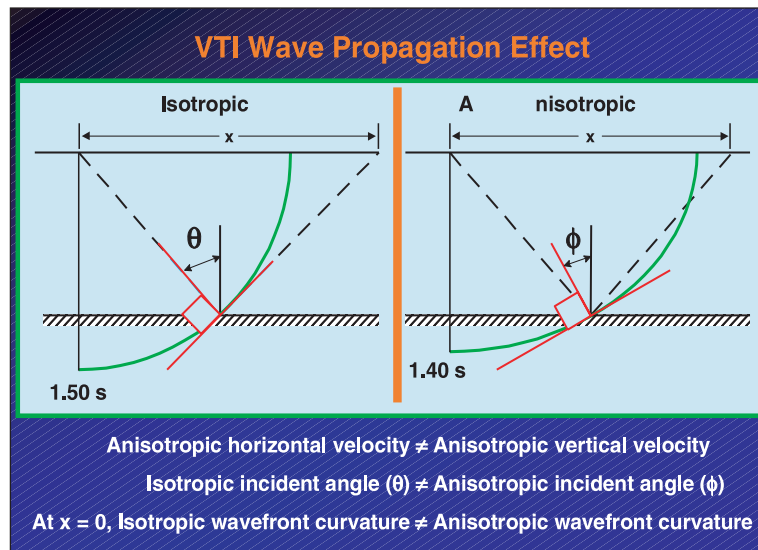


Figure 3.E.3

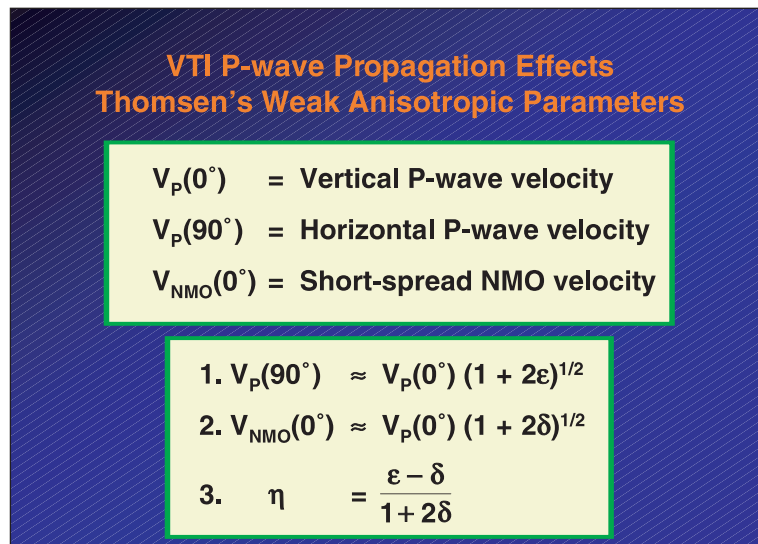


Figure 3.E.4

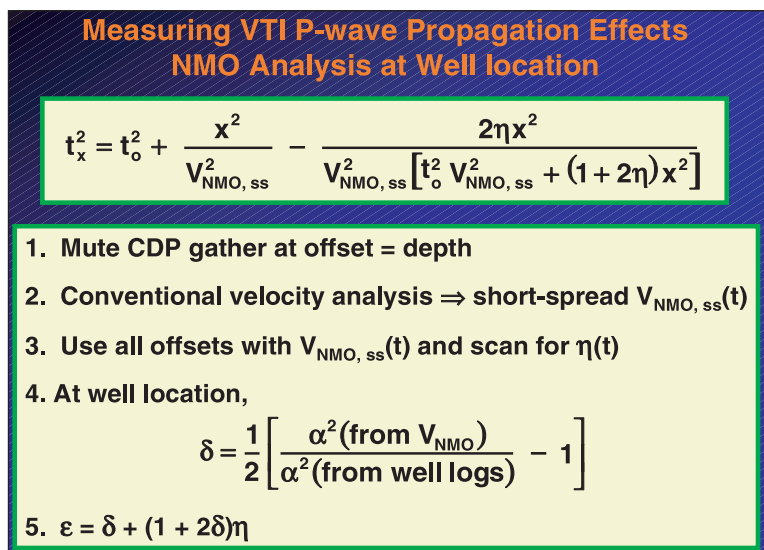


Figure 3.E.5

